STUDIES OF STRUCTURAL AND OPTICAL VARIATIONS OF NANOSIZED TiO_2 INDUCED BY PRECIOUS METAL DOPANTS (Au, Pt, Pd and Ag)

MASTER OF SCIENCE

in

PHYSICS

R. J. MOLOANTOA

2016

STUDIES OF STRUCTURAL AND OPTICAL VARIATIONS OF NANOSIZED TiO_2 INDUCED BY PRECIOUS METAL DOPANTS (Au, Pt, Pd and Ag)

By

RAMODIKA JACOB MOLOANTOA

DISSERTATION

Submitted in fulfilment of the requirements for the degree of

MASTER OF SCIENCE

in

PHYSICS

in the

FACULTY OF SCIENCE AND AGRICULTURE

(School of Physical and Mineral Sciences)

at the

UNIVERSITY OF LIMPOPO

SUPERVISOR: Prof. K.E. Rammutla

CO-SUPERVISOR: Dr. T.E. Mosuang

EXTERNAL CO-SUPERVISOR: Prof. T. Hillie (CSIR)

2016

DECLARATION

I declare that the dissertation hereby submitted to the University of Limpopo, for the degree of Master of Science in Physics has not been submitted by me for a degree at this or any other university; that it is my own work in design and in execution, and that all material contained herein has been duly acknowledged.

_____ _____

Moloantoa R.J. (Mr.) **Date**

DEDICATION

"Keeping my dreams thriving, Understanding that to achieve anything requires faith and believing in oneself, hallucination, self-discipline, effort, fortitude, and perseverance, remembering that all things are possible for those who believe."

This dissertation is dedicated to the following people: my mother Nkele, my father Mohlabeng, my wifes Mmakgolla, Refilwe, Kedibone and more over to my sons and daughters'. This dissertation is also dedicated to the friendship and loving memory of Prof. Kwena Rammutla my late supervisor for this work and my late grand-father Makgakga Tshekere & mother Manewa Mmamotsoko.

ACKNOWLEDGEMENTS

I wish to thank my late supervisor Prof KE Rammutla for the warm and skilful way in which he introduced the subject of this work. Not only did he provide guidance, assistance and constantly uplifted my morale, but he also believed in my potential and trusted that I will succeed even though I had problems during my educational path.

My sincere gratitude also goes to my co-supervisors Dr TE Mosuang and Prof. KT Hillie (CSIR) for their everlasting support, guidance and motivation during my research work.

I would like to thank my colleagues and friends for their encouraging words during hard times. It was highly rewarding to work with them.

I would also like to acknowledge Dr. RM Erasmus for helping me with Raman and DRS measurements at Wits laboratory.

I am also indebted to Tom Malwela's willingness to provide me with some technical training on SEM and AFM characterization techniques.

Special appreciation is given to Kenneth Kgatwane and Refilwe Ramohlale for their friendship and words encouragement and also for sharing both my happiness and sadness.

I am indebted to my entire family for their overflowing supports during the long difficult research process, namely, my brothers, Tshabedi and Kobang; my mother, Nkele and my father, Mohlabeng. I also would like to thank my brave beautiful wife's for their endless charitable love, support, total responsibility, trust and motivational words.

Financial support from NRF is highly appreciated and University of Limpopo appreciated for making time, space and guidance available for me to carry out my research.

TABLE OF CONTENTS

LIST OF FIGURES

LIST OF TABLES

ABSTRACT

Titania is a cheap and nontoxic polymorphic material of current interest for a variety of technological applications like in gas sensing and photovoltaic cells. Generally, TiO_2, with a band gap of 3.2 eV, can only be excited by a small UV fraction of solar light, which accounts for only 3-5% of the solar energy. Various strategies have been pursued including doping with metallic elements (e.g. Fe) or nonmetallic elements (e.g. N) with the aim of shifting the absorption into the visible range.

Since the properties and performance of devices, particularly for high-temperature applications, may be affected by the transformation from one phase to another, it is of significant interest to understand the conditions that affect phase transitions. In the present work TiO_2 was doped with platinum (Pt), palladium (Pd), silver (Ag) and gold (Au) at doping levels of 5% weight, following the standard sol-gel methods. Structural characterization was carried out using scanning electron microscopy, Raman Spectroscopy and X-ray diffraction. Optical properties were studied using the Diffused reflectance Spectroscopy (DRS).

Doping with Pt and Pd resulted in a lower anatase to rutile phase transformation temperature while doping with Au and Ag did not affect the transformation temperature. SEM micrographs show that the surface contains irregular shaped particles which are the aggregation of tiny crystals at lower temperature range, whereas at higher temperatures (900 °C), spheroids are observe.The reflectance spectra of the metal loaded TiO_2 reveal substantial strong spectral cut-off starting from roughly 400 nm to the entire visible region (i.e. they show enhanced absorption).

CHAPTER 1

1.1 GENERAL INTRODUCTION

Chapter 1 of this dissertation introduces the background information on the three phases of TiO_2, their structural importance and a wide range of applications while chapter 2 gives a basic review on structural aspects, particle size, impurities and precursor effects on phase transformation, and optical properties. The focus of this work was on the synthesis of titanium dioxide doped with precious metals (i.e. silver, gold, palladium and platinum) using the standard sol-gel method as outlined in chapter three, which also reflect the basic background on each characterization techniques and also to study the locations of dopants and their effects on the structural and optical properties.

Considerable interest in semiconductors of nanometer proportions has grown tremendously due to the quantum size effects that they exhibit [1]-[3]. Nano-crystalline semiconductors have electronic properties transitional between those of molecular entities and macro-crystalline solids and are at present the subject of intense research [4]-[9]. Nano-metric semiconductor particles exhibit interesting properties due to the large number of surface atoms and the three-dimension confinement of electrons [10].

Modifying both the size and shape of the particles can alter the degree of confinement of the electrons, and affects the electronic structure of the solid, in particular the band boundaries, which are tunable with particle size [10]. Nano-sized materials have been intensively studied due to their unique physical and chemical properties as well as their great potential of technological applications [4]-[8]. Regardless of many studies on the structural property relations of nanocrystallites using the several characterisation techniques, such an understanding is still to be acquired.

Therefore, the relationship between the size, phase transformation, metal dopants and the structure of TiO_2 nanocrystallites, which were prepared via a sol-gel method with titanium iso-propoxide Ti $[OCH(CH_3)_2]_4$ as the starting material will be explored. Titania has a wide range of applications in heterogeneous photocatalysis, including air purification, water treatment, self-cleaning, antifogging [11]. The material properties of TiO_2 nanocrystallites are a function of the crystal structure, nanocrystallite size, and morphology and, hence, are strongly dependent on the synthesizing method [11]-[20].

Titanium dioxide exists in three main kinds of crystalline structures namely anatase, brookite and rutile. The three possess different physical and chemical properties which direct them to different technological applications. For example, the anatase phase is suitable for catalysis, while the rutile one can be used in optical and electronic devices due to its high refractive index and dielectric constant [11]. The rutile phase is thermodynamically more stable than the anatase one at ambient temperatures. However, in the form of nanocrystallites and at low temperatures, the anatase structure is the stable phase [21].

Recently, nanostructured anatase TiO_2 has attracted much attention as a key material for dye-sensitised solar cells [21] and in gas sensors [22]. The applications of nanosized anatase TiO_2 are primarily determined by its physiochemical properties such as crystalline structure, particle size, surface area, porosity and thermal stability.

At very small particle dimensions, the surface energy is an important part of the total energy and it has been found that the surface energy of anatase is lower than that of rutile and brookite [23]-[26]. Although many attempts have been made to control the process of phase transformation in titania, the transformation occurs over a range of temperatures due to the complexity of the crystal growth during the sample calcining process.

One other route of inducing the phase transformation is by adding transition metal dopants which produces crystal defects and surface modifications which result in the change of transformation activation energy [27], [28]. Metal loaded

TiO_2 has been primarily studied to improve the catalytic activity under UV irradiation [29]. Numerous metal ions have been investigated but there are conflicting results on their effects on the visible-light photo-activity of TiO_2.

In the present work, focus will be on the synthesis of sol-gel derived TiO_2 doped with four different precious metals (Ag, Au, Pd and Pt) and studies of the effects of these precious metals on the structural and optical properties. The study is also aimed at establishing the locations of dopants i.e. whether they are in the TiO_2 matrix or on the surface regions.

1.2 STUDY OBJECTIVES

The objectives of the study are as follows:

- Synthesis of titanium dioxide nanostructures doped with Pt, Pd, Au and Ag using the sol-gel method.
- Characterisation of samples using X-ray diffraction (XRD), Scanning Electron Microscope (SEM), Raman Spectroscopy (RS) and Diffuse Reflectance Spectroscopy (DRS).
- Determination of dopant location (i.e. establish whether the metals go into the TiO_2 matrix or not.
- Determination of the effects of dopants on the optical properties of TiO_2.

1.3 DISSERTATION LAYOUT

Chapter 1 details the overall background on TiO_2 sol-gel synthesis, doping effect, the relationship between the size, phase transformation, metal dopants, the structure of TiO_2 nanocrystallites and the focus of this work.

Chapter 2 presents TiO_2 literature review looking at the particle size effect, the importance of starting precursor materials and effect of impurities on phase

conversion. It also outline the important application of TiO_2 in gas sensing, photovoltaic cells and includes the optical properties.

Chapter 3 informs about the starting precursor solutions used in this work and the history of each characterization technique employed.

Chapter 4 presents the overall results obtained and all calculations done during the experimentation including the observational confirmation of each technique employed during the investigations by one another.

Chapter 5 gives the research summary and conclusion.

CHAPTER 2

LITERATURE REVIEW

2.1 STUCTURAL ASPECTS OF TiO_2

Titanium dioxide has three polymorphs: rutile (tetragonal), anatase (tetragonal) and brookite (orthorhombic). In addition, there are two high pressure phases, TiO_2-II and TiO_2-III. Only the rutile, anatase and brookite will be described here as they are the main crystalline structures of TiO_2. The basic unit cell structures of these phases are shown in figure 1 (a), (b) and (c). Both rutile and anatase have a tetragonal structure, consisting of six and twelve atoms per unit cell, respectively. In both structures, each Ti atom is coordinated to six O atoms and each O atom is coordinated to three Ti atoms.

In each case, the TiO_6 octahedron is slightly distorted, with two Ti-O bonds slightly greater than the other four, and with some of the O-Ti-O bond angles deviating from 90^0. The distortion is greater in anatase than in rutile. Both crystal structures are frequently referred to as chains of TiO_6 octahedra having common edges [30] with two and four edges shared in rutile and anatase, respectively. Brookite was first discovered in 1849 in Magnet Cove [31], a site of large deposits of the mineral. It was originally named ‘arkansite’ for the state it was discovered in, Arkansas. The brookite structure is more complex and has a larger cell volume when compared to the other two polymorphs. It is a highly unstable phase amongst the three phases of TiO_2; its unit cell is made of eight formula units of TiO_2 and is formed by edge distribution TiO_6 octahedra which are similar to rutile and anatase structures [6]. Brookite is transitional in density between rutile (densest) and anatase. It is of lower symmetry, orthorhombic, versus tetragonal for rutile and anatase. TiO_2 short-range order is less regular;

in brookite, all six nearest-neighbor Ti–O bond lengths are different and the values span a larger range than in the tetragonal forms [5]. Studies of amorphous TiO_2 suggest a closer relation to brookite than to anatase and rutile crystal forms of titania [32].

In the TiO_2 lattice structure, two sites (interstitial and substitutional) are identified, and dopant elements can occupy the sites relative to thermal treatment of the samples [33]. There seems to be a general agreement in the literature that the dopants that increase or create a high concentration of oxygen vacancies in TiO_2 will accelerate the anatase to rutile phase transition whereas dopants that reduce such vacancies will stabilize the anatase phase [34].

So far, it has not been possible to predict the effect of a given element on this phase transition based on its position in the periodic table. Whereas copper is known to accelerate the anatase to rutile phase transition [35, 36], gold has been reported to retard it [37].

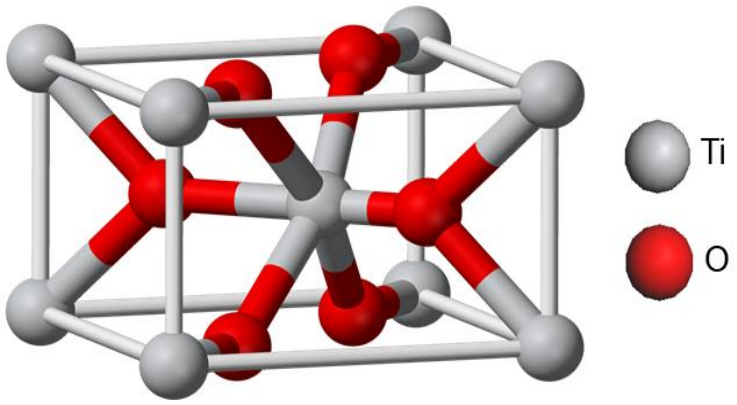

Figure 2.1 (a): The crystal structures of a rutile titania polymorph

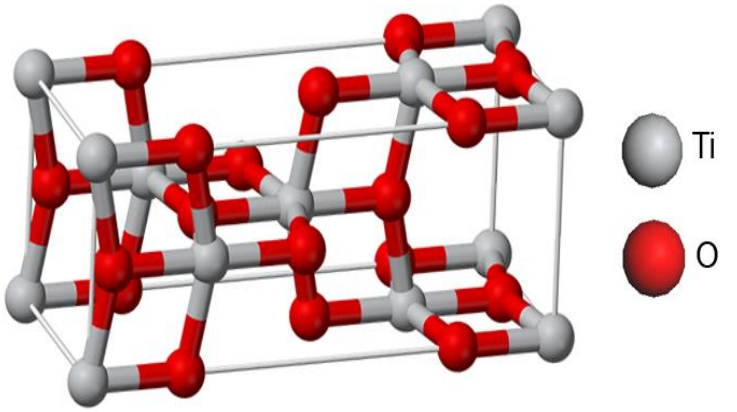

Figure 2.2 (b): The crystal structures of anatase titania polymorph

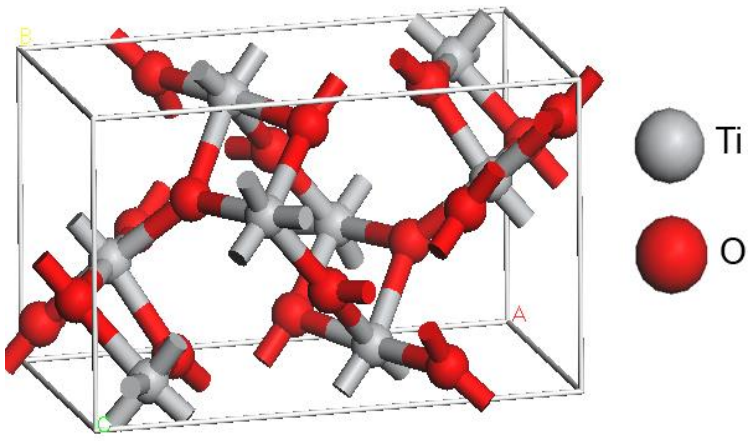

Figure 2.3(c): The crystal structures of brookite titania polymorph

2.1.1 Particle size effect of on phase transformation

Size reduction in nanocrystalline TiO_2 leads to various exciting phenomena due to the enhanced surface to volume ratio and the length scale for both mass and charge transport since size effect refers to the change in thermodynamic stability. Previous reports showed that in bulk TiO_2 rutile is stable however, in nano TiO_2; the competition between surface energy and the energetic of polymorphs stabilizes anatase at smaller particle sizes which the result in thermodynamic stability CROSSOVER between anatase and rutile phases noted by Wang *et al*. in (2013) [38].

There are two main grain size effects on phase transition which are involved that will be deliberated in this subdivision. The "critical particle theory" is considered generally as thermodynamic theory which was explained originally by Garvie in reference to zirconia system in (1978) [39]. This theory was applied by Kumar in (1995) [40] on the titania system, although the particle size kinetic energy effect on phase transition from anatase to rutile was suggested by Gribb and Banfield in (1997) [41]. Zirconia system is comparable to Titania system in many ways, which has a tetragonal to monoclinic phase transition. Size effect critical theory was deliberated by Garvie [39]. Free energy of a specific crystal of ZrO_2 is as follows:

$$\mathrm{GT} = \frac{4}{3}\,\pi \mathrm{r}^3 \mathrm{GVT} + 4\pi \mathrm{r}^2 \gamma \mathrm{T} \qquad (2.1.1.1)$$

With GT = tetragonal phase free energy, GVT = tetragonal phase volume free energy, r = particle radius, and γ = surface energy. Similar expression of monoclinic phase can be detailed as having a different free energy as below:

$$\Delta \mathrm{G} = \frac{4}{3}\,\pi \mathrm{r}^3\,\Delta \mathrm{GVT} + 4\pi \mathrm{r}^2 \Delta\gamma \qquad (2.1.1.2)$$

When tetragonal and monoclinic phases are in equilibrium, ΔG = 0 hence the radius is as follows:

$$\mathrm{r} = -\frac{3\Delta\gamma}{\Delta \mathrm{GV}} \qquad (2.1.1.3)$$

If the free volume energy is defined as:

$$\Delta \mathrm{GV} = \Delta \mathrm{H} - \mathrm{T}\Delta S \qquad (2.1.1.4)$$

and knowing that ΔGV=0, at equilibrium the transformation entropy is expressed as follows:

$$\Delta S = \frac{\Delta H}{T_b} \tag{2.1.1.5}$$

T_b = equilibrium transition temperature

Equations 2.1.1.4 and 2.1.1.5 can be joined to give

$$\Delta GV = \Delta H - \frac{T\Delta H}{T_b} \tag{2.1.1.6}$$

From equations 2.1.1.3 and 2.1.1.6, critical particle size is defined as:

$$r_c = \frac{-3\Delta\gamma}{\Delta H\left(1-\frac{T}{T_b}\right)} \tag{2.1.1.7}$$

The particle radius that prevents transition of tetragonal to monoclinic phase is defined as Garvie's critical particle size. Depending upon the fact that monoclinic phase have a higher surface free energy compared to tetragonal phase, if not, size effect would not be there [39]. After the suggestion by Garvie, Srinivasan *et al*. in (1990) [42] markdown the effect of critical size and ascribe that to zirconia stabilization due to chemical factors, furthermore it was also acknowledged that if the minimum particle size are smaller then the theory becomes more effective and it can be considered.

The rate of transition between tetragonal to monoclinic constantly fast-tracks due to an increasing particle size hence the phenomena can mostly be explained using the possibility that, an existing nucleus responsible for transformation rises with an increase of tetragonal phase volume, which hence becomes interpreted as greater grain size. A further clarification offered is that during particle growth, flexible stresses have a tendency of appearing, which are known to promote this tetragonal to monoclinic phase transformation [42]. The critical size effect as it applies to titanium dioxide is summarized by Kumar [42], who used it to explain the initiation of the anatase-rutile transformation. He found that both the grain sizes of rutile and the rutile content increased with increasing time and calcination temperatures. The total free energy change upon nucleation or growth processes can be expressed as:

$$\Delta G = \frac{4}{3}\pi r^3 g_V + 4\pi r^2 g_s + \frac{4}{3}\pi r^3 g_e \quad (2.1.1.8)$$

r = nucleus radius, g_v = free energy volume variance/ unit volume, g_s = required energy for new surface/unit area, and g_e = free energy for mechanical and environmental stress effects. The nucleus is considered to be stable under critical nuclei size effect theory if it reaches the critical size r_c. If all is considered to be uniform, nucleus critical size will only depend on transitional energies considered, as below:

$$r_c = \frac{-2g_s}{g_V + g_e} \quad (2.1.1.9)$$

which was used by Kumar to give details about the observed increase in rutile grain size upon meta stable to stable transformation (i.e anatase to rutile). In a stress-free environment g_e is considered to be less or equals to 0, which is true because of the decrease in volume during phase transition from anatase to rutile of 8% which results because of thermodynamic effects as reported by Gribb and Banfield in (1997) when investigating the kinetic effects of particle sizes on TiO_2 [41].

It was found that substantial effect of grain size on anatase to rutile transition rate in nanocrystalline TiO_2 was due to the fact that an increase in rate of reaction was related to the decrease in grain size [41]. The possible three special rate limiting factors which point out a dynamic concern relating to the particle size effect that has a change in reaction rate explained as below:

1) Possible Nucleation sites.

Because of pure geometric special effects, total number of promising nucleation surface sites/unit volume upturns by a reduction in grain size. As the number of possible sites per unit volume increases, it will practically mean that if the amount of surface nuclei raises then the degree of phase transition will increases as well depending on the elemental reactivity.

2) Dynamic (Energy) Force.

The dynamic force of phase transition can be considered as a variation in free energies amongst reactants and products stages. Gribb and Banfield in (1997) [41] quoted studied the investigations and provided suggestive evidence indicating that rutile has a higher surface energy than anatase and hence this suggest that driving (dynamic) force decrease with an increase in particle size which then reduce the rate of reaction. This is in line with the investigated data delivered by Gribb and Banfield in (1997) [41] and it was hence considered as an enhanced clarification.

3) Stored Energy.

The rutile molar volume is between 8-10% which is less than that of anatase molar volume, which then suggest the possibility of a strain energy linked to the phase transition. Variation in hydrostatic-like pressure and surface tension on less crystallites may influence the stored (strain) energy.

The decrease in grain size influences hydrostatic-like pressures and surface tension to potentially decrease the stored energy hence decreasing one of transition barriers. Considering the data reported by Gribb and Banfield in (1997) [41] that incorporated the investigation of both macrocrystalline and nanocrystalline titania.

2.1.2 The effects of sol-gel precursor on phase transformation

The process of sol-gel can be demarcated as the formation of an oxide through polycondensation reaction of a molecular precursor in liquid and regarded as a versatile process in various ceramics [43]. In a typical sol-gel process, a stable dispersion of colloidal particles in solvent is formed called a sol followed by a three dimensional continuous network that extends across the entire container called a gel [44].

After the gel is formed, numerous sol particles and cluster will still co-exist with the gel in the container hence aging becomes an important stage since the liquid phase still contains sol particles and agglomerates which will continue reacting till the gel dries [45]. Dehydrating of the gel normally leads to a

malformed structure due to capillary forces dragging the walls of the pores together and dropping the pore size. The growth rate of different TiO_2 nanocrystallites crystal planes with specific absorption of shape controllers to these planes can be recognized as shape control process under different pH condition [43].

A lengthy drying period of the as-prepared gel helps in evading the agglomeration of TiO_2 nanocrystallites during the crystallization process. Calcining the amorphous TiO_2 in air forms a single phase TiO_2 nanocrystallites with an average size ranging from 7 to 50 nm as reported by X. Chen and S. S. Mao [46] in (2007).

In sol-gel a lot of information regarding various advantages paralleled to the conventional powder route, such as, low temperature processing, high purity, level of molecular homogeneity in materials and submicron particle size [47]. The standard sol-gel room temperature process the entrapment of organic molecules that are associated to optical transparency within the matrices provide optical properties (i.e. absorbance, reactance, bandgap narrowing etc.) that are vital [43]. These powders find applications in the ceramic industry when high performance materials are required. Sintering time and temperature can be significantly reduced with powders of narrow particle-size distribution. Fine colloidal particles can be made by a variety of methods from the vapour phase or the liquid phase [48]. The sol-gel process offers new approaches to the synthesis of fine powders [49]. Starting from molecular precursors, the oxide network is obtained by inorganic polymerization reactions [13], [49].

The effects of sulfate and chloride solutions were studied and reported by Wilska *et al.* in (1954) [50]. It was found that the initially dried products were always amorphous. It was also suggested that the first crystalline forms present are influenced by the preparation method and the precursor of the starting solution. Further established was that samples prepared from solutions of sulfate are in most cases found to be in anatase phase, while boiling chloride solutions mostly gives rutile phase [51].

Wilska *et al*. (1954) [50] found in most cases amorphous phase exist prior to the crystalline phase even during direct rutile formation. There has not been a proposed mechanism suggested to clarify the various effect of chloride or sulfate precursors on phase transition. There are different starting solutions that can be used in the preparation of titanium dioxide nanopowders [50], [52].

Dambourmet *et al.* in (2010) [52] used titanium oxysulfate-sulfuric acid complex hydrate ($TiO_2SO_4.H_2O.H_2SO_4$) as a precursor for the preparation of TiO_2 nanopowders under a strong acidic medium of pH 0.1 and found that the agglomerates of nano-size TiO_2 particles were of anatase phase. It was further suggested that the sulfate species act as a directing agent that favors the formation of anatase at the expense of the thermodynamically stable phase (rutile).

A further clarification was that using titanium tetra-isopropoxide, formic acid and Silver nitrate to prepare Ag-TiO_2 nano powders, it was established that the as-prepared sample was amorphous even after annealing at 300 °C and suggested that there is a promotion in phase transformation caused by a decreasing anatase grain size due to an increase in the total boundary energy of the TiO_2 powders [52].

Li and Zeng in (2011) [53] used hydrolysis of $TiCl_4$ in sulfuric acid as a starting precursor and found that the presence of certain amount of H_2SO_4 enhance anatase formation and phase transformation at about 600 ˚C. The group concluded that both calcination temperature and hydrolysis temperature have important effects on phase transformation and particle size. Bessekhouad *et al.* in (2003) [54] prepared titanium dioxide nano-powders using tetra-isopropylorthotitanate Ti $(OC_3H7)_4$ as a starting precursor for the sol-gel synthesis and concluded that this route lead to only anatase phase being observed at lower temperatures. It was also reported by Lao *et al.* in (2005) [55] that it was possible to prepare almost pure anatase nano-TiO_2 from mixed-solvent-thermal method (MST) using $TiCl_4$ as the starting material which can produce almost 10 nm particle size at the temperature range of 80 to 100 °C for drying the reference sample. The conclusion made from this investigation was that the method helps in the high performance of the DSSCs [55].

2.1.3 The effects of impurities or dopants on phase transformation

Shannon and Pask in (1965) [56] studied the impurities influence on growth and nucleation on transformation from anatase to rutile. They concluded that processes that create oxygen vacancies, such as the addition of acceptor dopants (ions with a lower valence that $Ti^{4+)}$ and use of reducing atmospheres accelerate the anatase-rutile transformation.

Conversely, processes that increase the concentration of titanium interstitials, such as the addition of donor dopants, inhibit the transformation. Shannon and Pask hypothesized that an increase in the concentration of oxygen vacancies reduces the strain energy that must be overcome before the rearrangement of the Ti-O octahedra can occur, and that cations with a valence less than that of titania ($^{4+}$ ion) will increase the concentration of oxygen vacancies, due to the necessity for charge balance.

The presence of dopants in the creation of nano-doped-TiO_2, have the effect on phase transformation from anatase to rutile, which is prevented when the thermal energy is low enough to overcome the nucleation barrier during the thermal dehydration process, and this occurs more readily with the smaller crystallite size of nano-doped-TiO_2 [57].

In short, dopants overpower the crystallite growth of nano-TiO_2 by inserting itself or themselves into the lattice structure of the nano-doped-TiO_2 octahedral to modify its physicochemical properties. Some researchers claim that the presence of dopants do not affect the morphology of nano-doped-TiO_2 [58, 59]. For example, Nahar *et al.* in (2009) [58] noted that Fe dopant at dopant level ranging from 0-10% did not have any change in the phase transformation of doped TiO_2 nano powders prepared by calcination method. Li *et al*. in (2006) [59] claimed that cerium ions had no obvious effect on the particle size, morphology, and crystalline phase of nano-doped-TiO_2.

The focus of the present work will be on the structural and optical effects brought about by precious metal dopants (palladium (Pd), silver (Ag), platinum (Pt) and gold (Au)) in TiO_2. Palladium (Pd) and silver (Ag) have been investigated by Wu *et al*. in (2004) [60] to enhance the photocatalytic performance of nano-doped-TiO_2 using the dopant mole ratio of 0.1, 0.2, 0.05 and noted that dopant levels impact on crystallinity, absorption threshold and the interaction between metal ions with TiO_2. Among the transition metals dopants confirmed, Pd ion had the strongest interaction with nano-TiO_2 and improved its morphology most commendably. In the present study dopant levels are higher i.e. 5%.

The performance of nano-TiO_2 was examined by Sakthivel *et al*. in (2004) [61] [who introduced a noble metals such as platinum (Pt), gold (Au) and palladium (Pd) dopants which acted as an electron trappers during the formation of TiO_2; by decreasing its surface area. The generated free electrons dropped towards metals which served as temporary electron trappers preventing electron-energized holes recombination. The increased Pt content also competed with TiO_2 as an electron trap to decrease the effective surface area at last. A further increase in Pt dopant might lead to the following possibilities:

(1) Shortening of the charge carrier space distance [61],
(2) Recombination of free electron and energized hole [62],
(3) Agglomeration of Pt and TiO_2 [63], and
(4) Decrease in the probability of oxygen being photo-adsorbed on TiO_2 [63].

2.1.4 Anatase to Rutile transformation

In this work, our goal is to study the anatase-rutile phase transformation after a series of heat treatment and addition of noble metals into TiO_2 matrices prepared by standard sol-gel process. To accomplish that goal, we employed physical absorption, X-ray diffraction and Raman spectroscopy techniques. In archiving the goal successfully, one should understand the factors that control the phase stability, growth and phase transformation kinetics in nano-TiO_2 which is important for quantifying the behaviour of TiO_2 material.

The three polymorphs Titania can be crystallized at low temperatures as ultrafine particles depending on the preparation conditions. The factors in consideration will determine how phase composition, microstructure and the properties of titania-based materials can be manipulated as reported by Zhang and Banfield in (2000) [64].

Hu and co-workers in (2003) [65] pointed out that the anatase to rutile phase transformation (ART) in TiO_2 is an area of both scientific and technological interest and that is one of most important parameters in determining the properties of the material such as sensing and photocatalytic properties [65]. The anatase to rutile transformation (ART) is kinetically defined and the reaction rate is determined by parameters such as particle shape, size and oxygen defects [65]. According to previous findings as suggested by Grzmil and his group in (2013) [66] the activation energy for anatase to rutile phase transformation involves the activation energy of coarsening of anatase particles, the activation energy of nucleation, and the activation energy for the nuclei growth. The group further found that an increase in the degree of anatase to rutile transformation for both temperature and calcination time, depended mostly on the type of the in-cooperated modifier.

The anatase titania nano-crystals grow and then transform to rutile only when a critical size and temperature is reached, which is a contribution made by B Grzmil *et al.* in (2013) [66]. Rutile is the thermodynamically stable phase, while anatase and brookite are both metastable; transforming to rutile under heat treatment at temperatures typically ranging between 600 – 700 °C.

Anatase is widely regarded as the most photocatalytically active of the three crystalline structures of TiO_2 as reported by Masuda and Kato in (2009) [67]. The generally accepted theory of phase transformation is that two Ti–O bonds break in the anatase structure, allowing rearrangement of the Ti–O octahedra, which leads to a smaller volume, forming a dense rutile phase as suggested by Cloudhury and Cloudhury in (2013) [68].

Breaking these bonds can be affected by a number of factors, including the dopants addition, synthetic method and thermal treatment [68]. The removal of oxygen ions, which generate lattice vacancies, accelerates the transformation by following the first order kinetics as noted by Uberuaga and Bai in (2011) [69]. It was further suggested by the group that the defect kinetics differs in anatase and rutile, with interstitial species diffusing quickly in rutile while oxygen defects (i.e interstitial and vacancies) are fast diffusers in anatase.

2.2 TiO_2 FOR GAS SENSING DEVICES

A gas sensor is a device that creates an electrical signal in response to a chemical interaction with vapor or gases. Such a device offer low cost, high sensitivity, fast response and advantages that would promote use as new applications emerge, mostly in environmental control as noted by Korotcenkov in (2008) [70].

It was further established that the working principle of a typical resistive metal oxide gas sensor is based on a shift of the equilibrium state of the oxygen surface reaction due to the presence of the target analyte; the effective change in concentration of chemisorbed oxygen is then recorded as a change in the resistance of gas-sensing material [70].

In doped semiconducting oxides the sensing parameters such as selectivity, sensitivity and operating temperature can be improved by addition of metals. The detection mechanism of systems involves changes in electrical conductivity in the present of reducing or oxidizing gases due to catalytic oxidation or reduction at the metal oxide surface.

In these types of sensors, the catalytic reaction depends on their electronic structure, chemical composition, crystal structure and the morphology of the surface which is exposed to the gas as reported by Esfandiar *et al*. in (2012) [71]. Hoel *et al*. in (2005) [72] established two imperative groups of sensors used as detection of individual gases such as (NO_x, NH_3, O_3, CO, CH_4, H_2, SO_2, etc.) and generally the monitoring of changes in the environmental atmosphere.

The group investigated the effect of dopant and annealing temperature on the sensitivity of undoped and Pd-WO_3 gas sensors [72] and in their deliberation it was put forward that doping improved the sensing properties of WO_3. Single gas sensors can, for example, be used as fire detectors, leakage detectors, controllers of ventilation in cars and planes, alarm devices warning of an increasing threshold concentration value of hazardous gases within work places.

Hazra and Basu in (2006) [73] experimented by aluminium doped titania thin films using thermal oxidation and further coated it with palladium. They found that the improvement in sensitivity with increasing hydrogen concentration is due to the involvement of more palladium active sites at higher partial pressures of hydrogen.

The detection of volatile organic compounds (VOCs) or smells generated from the foodstuffs or household products has also become increasingly important in food industry and in indoor air quality, and multi-sensor systems (frequently denoted to as *electronic noses)* are the modern gas sensing devices intended to analyse such complex environmental mixtures as indicated by Capone *et al.* during the group‘s (2003) [74] research contribution.

Due to a changing environmental safety regulation, the detection of hazardous, harmful, or toxic gases has become very significant. Significantly, reproducible gas sensor devices with enhanced features have become a stimulating research area.

Above and beyond exhibiting, reversible, rapid and reproducible respond, a gas sensor should meet the following important factors which are continuously investigated for better performance.

- High sensitivity, which refers to a noticeable signal even in the presence of a small concentration of a specific target gas at high and low temperatures.
- High selectivity towards the target gas.
- Stability, both chemical and mechanical, for extended periods, often in harsh environments such as an automobile exhaust.

- Durability, which is its utility to last for an elongated period without the sensor device losing its sensing ability.
- Cost effective to both producers and consumers.

2.3 TiO_2 FOR PHOTOVOLTAIC CELLS

Due to an improvement in the world's economy; the need of energy is drastically increasing because of inhabitants and industrial growth. The Current primary energy consumption in the world is close to $4.7\ X\ 10^{20} J$ per annum and it is estimated to grow by 2% each year for the next 25 years as projected by Goncalves *et al*. in (2008) [75]. Almost 90% of the world energy is sourced from fossil fuels which are mainly produced from oil, natural gas and coal, however these natural resources will be depleted in this century given today's rate of energy need [75].

The research further pointed out that in addition to the demand of energy, there are other problems such as pollution and climate change which associates to the burning of fossil fuels and regulatory precautions should be implemented. Therefore energy subject is and will continue to be the focal point of discussion in research and green economy.

The development of renewable and clean energies sourced from wind, solar, and water is required. It is of strategic importance in the environmental sustainability. Among these renewable energy sources, photovoltaics have been used commercially for more than half a century and is still one of the hottest topics in today's research and development. Photovoltaic devices convert solar irradiation directly to electricity with zero emission of hazardous gases and it has the potential to supply the whole world's energy demand as noted by Kelvin *et al*. in (2012) [76].

To address the problem of the production of solar cells at high temperature and fabrication cost the current research focuses on a new technology called Dye-sensitized solar cells (DSSCs). The dye-sensitized solar cell (DSSCs) are third generation photovoltaic devices that holds major promise for the economic

conversion of solar energy to electrical energy, because of the use of inexpensive materials and a relatively simple fabrication process.

In DSSCs according to Huang *et al*. in their (1997) [77] experimentation report, the dye molecules absorb visible light, and inject electrons from the excited state into the metal oxide conduction band. The injected electrons travel through the nanostructured semiconductor to the current collector, and the dye is regenerated by an electron donor in the electrolyte solution.

The DSSCs are fully regenerative, and the electron donor is again obtained by electron transfer to the electron acceptor at the counter electrode [77]. The group pointed out that the photocurrent density (J_{ph}) observed is given by the equation below:

$$J_{ph} = J_{inj} - J_r \qquad 2.4.1$$

where J_{inj} is the electron injection current resulting from the dye sensitization and J_r is the surface recombination current. The J_{inj} is related to the incident photon flux I_0 ($cm^{-2}s^{-1}$) by the expression:

$$\mathrm{J_{inj}} = qAI_0 \qquad 2.4.2$$

where q is the electronic charge and A is the ratio of absorbed photo flux to $I_{0.}$ The recombination current depends on the rate constant of back electron transfer k_{et}, the concentration of the oxidized half redox couple $C_{OX,}$ and the difference between the electron population in the semiconductor present in the dark n_0 and in light n so that J_r can be given by:

$$J_r = qk_{et}C_{OX}^{m}\,(n^{u\alpha} - n_0^{u\alpha}) \qquad 2.4.3$$

where the order of the rate of reaction is expressed as the exponents m for the oxidized redox species and u for electrons; α is the electron-transfer coefficient. Electron population (n) is related to the photo-voltage V by the equation below:

$$n = n_0 \exp[\tfrac{qV}{kT}] \qquad 2.4.4$$

where $qV = E_f - E_{f_0}$; E_f and E_{f_0} are the respective Fermi levels of TiO_2 in the light and in the dark.

A schematic presentation of the operating principles of the DSSCs is given in Figure 2.4 a) and b).

Otakwa *et al*. in (2012) [78] investigated the effect of air mass on the TiO_2 DSSC performance and found that the fill factor (FF) and solar – to - electricity conversion efficiency (η) increased with air mass (AM) while open circuit voltage V_{OC} and J_{SC} decreased. It was further noted by the group that for a maximum energy collection, solar collectors need to be tilted to an optimum tilt angle for capturing maximum radiation since photo-current density (J_{ph}) is influenced by air mass at a particular place. The air mass (AM) refers to the transverse path length by the direct solar radiation as a transverse path ratio to a point at sea level when the sun is directly above which helps in the determination of atmospheric refraction.

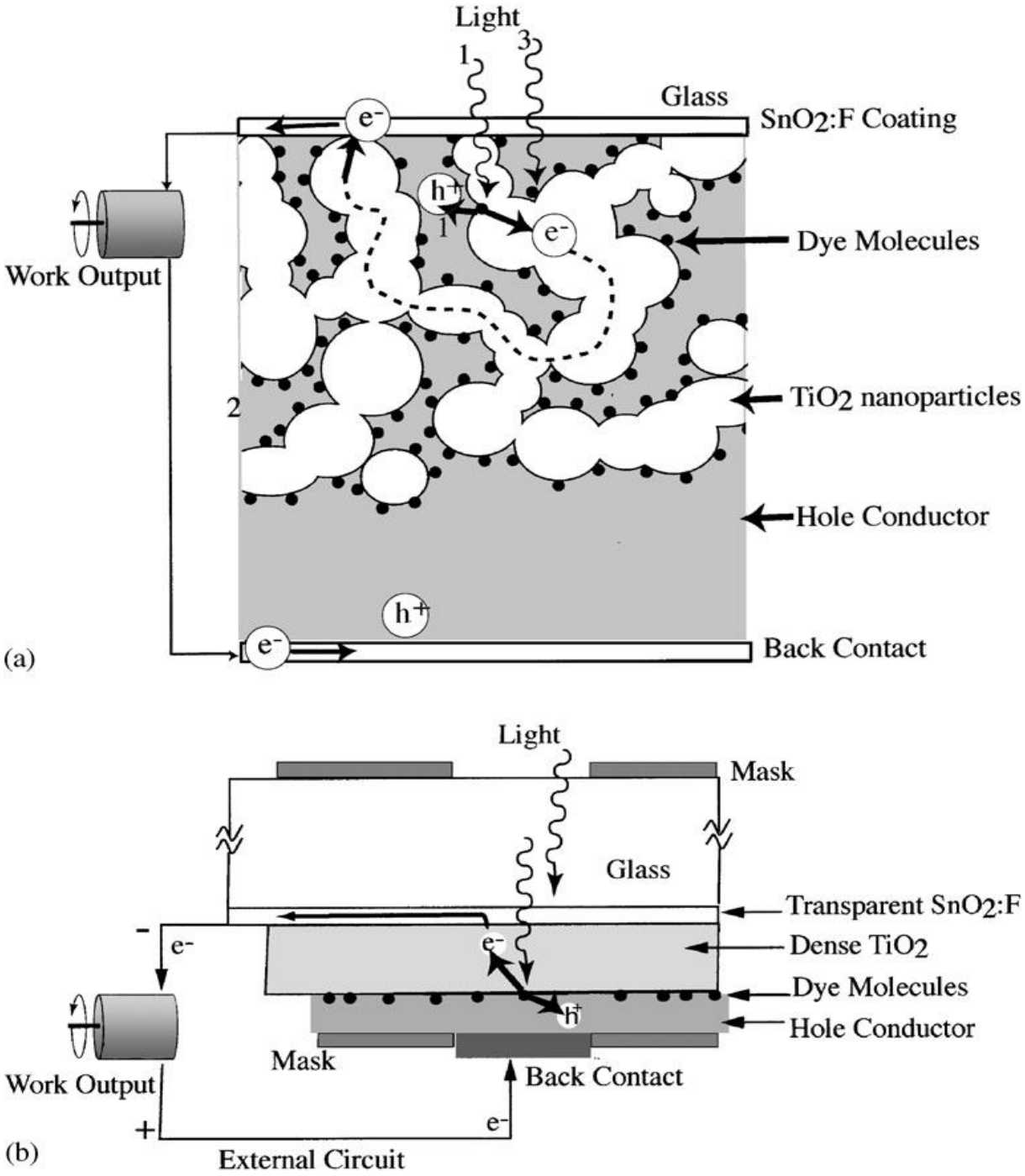

Figure 2.4: (a) A schematic diagram of the DSSC configuration using nano- or porous TiO_2 and (b) solar cell configured using non-porous TiO_2 and hole conductors [79].

Based on literature, Daghrir *et al*. in (2013) [80] reported that TiO_2 can be activate under UV irradiation having a wavelength lower than 387 nm due to its large band gap range of 3.0-3.2 eV which accounts 5% of solar energy while the visible light contributes 50%, hence that become a limiting factor. To overcome this limiting factor there is a need in shifting the absorbance by modifying the nano-crystalline TiO_2 through metal-doping as is considered to maximize the photocatalytic efficiency because of increased electron traps and decreased TiO_2 band gap by Ni *et al*. in (2007) [81].

Zaleska in (2008) [82] reported the importance of platinum group metals doping TiO_2 in enhancing the photocatalytic effect by improving trapping of electrons to inhibit electron-hole recombination during irradiation and that the major role of the metal dopants on TiO_2 is attributed to accelerating superoxide radical anion $O_2^{-\bullet}$ formation and also decreasing the effect of scavernging the electrons in the conduction band. The metal dopants localizes energy levels in the band gap of TiO_2 into which valence band electrons of TiO_2 are excited at wavelength longer than 400 nm.

2.4 OPTICAL PROPERTIES

The semiconductors optical properties have been studied extensively for their relevant application in solar cells, light emitting diodes, lasers and sensors. To understand these properties it worth considering the main mechanism of light absorption in pure semiconductors which can be defined as the direct interband electron transitions as suggested by Chen and Mao in (2007) [7] chemical review.

It was further established by the group that the absorption is small in indirect semiconductors such as TiO_2, where the direct electron transitions between the band centers are prohibited by the crystal symmetry. Braginsky and Shklover (2000) [83] have shown the heightening of light absorption in small TiO_2 crystallites due to the indirect electron transitions with non-conservation of momentum at the interface.

According to the group the absorption value and frequency depend mostly on the interface electron level not on its closeness to the band edge [83] and concluded that the effect increases at a rough interface when the share of the interface atoms is larger. The indirect transitions are allowed due to an outsized dipole matrix element and a large density of states for the electron in the valence band.

Substantial improvement of the absorption is expected in small TiO_2 nanocrystals, as well as in porous and microcrystalline semiconductors, when the portion of the interface atoms is sufficiently large. A quick increase in the absorption takes place at low ($h\nu < E_g + W_c$) photon energies, where W_c is the width of the conduction band [7]. Electron alterations to any point in the conduction band become possible when $h\nu = E_g + W_c$. Further enhancement of the absorption occurs due to an increase of the electron density of states in the valence band.

The interface absorption becomes the main mechanism of light absorption for the crystallites that are smaller than 20 nm noted by Brangisky and Shklover in (1999) [25]. Sato *et al*. in (2003) [84] showed through first-principles calculations and measurements within density functional theory (DFT) that the band gap of TiO_2 nanosheets was larger than the band gap of bulk TiO_2, due to lower dimensionality, i.e., 3D to 2D transition.

From the measurement, it was found that the lower edge of the conduction band for the TiO_2 nanosheet was approximately 0.1 V higher, while the upper edge of the valence band was 0.5 V lower than that of anatase TiO_2 [84].

CHAPTER 3

EXPERIMENTAL METHODS

3.1 PREPARATION OF PRECURSOR SOLUTIONS

The specific chemicals that were used in the study include: titanium tetra-isopropoxide ($Ti[OCH(CH_3)_2]_4$, TTIP, Aldrich, 97%), ethanol (CH_3CH_2OH, 95.96%), propanol ($CH_3CH_2CH_2OH$, 96.97%), methanol (CH_3OH, 95%) and nitric acid (HNO_3, 32%). The metal ion salts that were used in the preparations include: $AgNO_3$, $PtCl_4$, $AuCl_2$, and $PdCl_2$.

These metal ion salts were first dissolved in a minimum amount of water (H_2O) to form solutions before the additions of either of the alcohol solvents. Standard sol-gel methods were used to prepare the metal loaded TiO_2 nanocrystallites. Briefly, about 35 ml of TTIP was dissolved in 50 ml of ethal-1-ol. The required amount of metal precursor was then added and the mixture magnetically stirred for 10 min and then 5ml HCl solution was dissolved in 30 ml of butan-1-ol and mixed for 10 min.

The second solution was then added to the first and the whole was stirred for a further 60 min. These gels were then dried at 80 -100 ◦C for overnight. The dried sampless were ground to fine powders and divided into four potions, placed in quartz crucibles and calcined for 1 hour at different temperatures ranging from 300 – 900 ◦C.

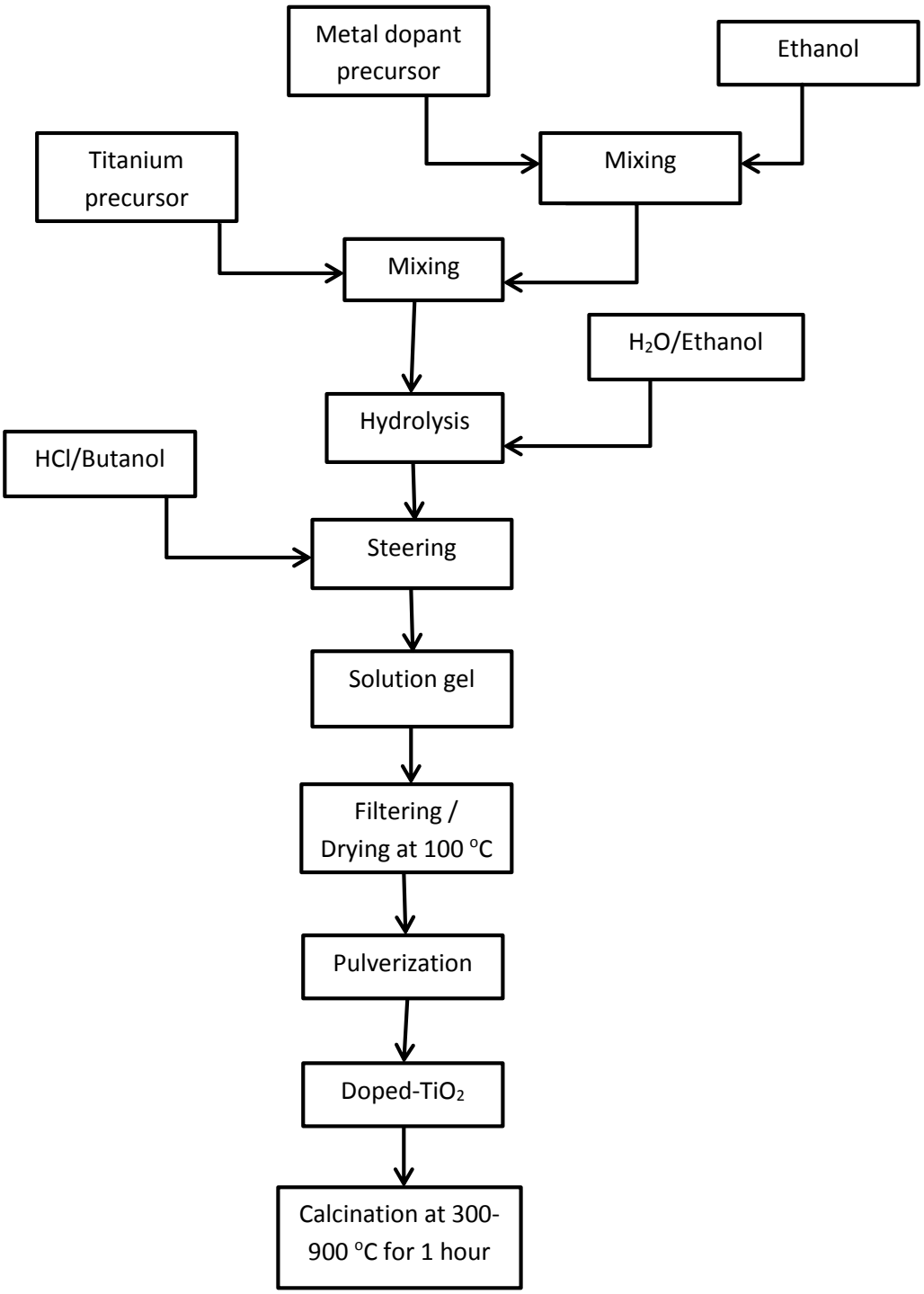

Figure 3.1: Typical procedure of metal doped-TiO_2 preparation by standard sol-gel method.

3.2 CHARACTERISATION TECHNIQUES

3.2.1 X-ray Diffraction (XRD)

XRD is one of the primary techniques used to characterize solid-state materials. It can provide valuable information about the crystalline phase and average crystallite size. When X-rays strike the sample, several processes take place like absorption, photo emission, florescence, as well as the emission of X-rays of high wavelength. Coherent and incoherent scattering from a crystal lattice can be observed from diffracted beams when the energy of the source X-rays is lower (1 keV-100 keV). The structure of a crystal is analyzed by the X-ray diffraction patterns. Bragg's law is the basis for X-ray diffraction (XRD), because it is related to the coherent and incoherent scattering. The Bragg's equation is as follows:

$$2d\mathrm{Sin}\theta = n\lambda \qquad (3.2.1.1)$$

where,

n =Order of a reflection (n = 1, 2, 3 ....).

λ = wavelength.

d = Distance between parallel lattice planes.

θ = Angle between the incident beam and a lattice plane, known as the Bragg angle.

The d spacing can be expressed through cell parameters and the Miller index by the following equation:

$$\frac{1}{d^2} = \frac{h^2}{a^2} + \frac{k^2}{b^2} + \frac{l^2}{c^2} \qquad (3.2.1.2)$$

where, d is the d-spacing; a, b, c are sides of the unit cell; and h, k, and l are the Miller indices, which are used to describe the lattice planes and directions in a crystal. XRD was performed utilizing conventional laboratory diffractometer, a Phillips PW1720, using a Cu K_α tube which can be expressed as follows:

$$\mathrm{CuK}\alpha_1 + \mathrm{K}\alpha_2 = 1.542\text{Å} \quad (3.2.1.3)$$

having a radiation with a power of 35 kV - 20 mA for the crystalline analysis. The broad-scan analysis was typically conducted within the 2θ range of 10 - 80°. The strongest peak for the anatase (101) and the rutile (110) phases of TiO_2 were used to estimate the average size of the metal oxide nano-crystallites using Scherer's equation [85]**:**

$$\mathrm{D_{crys}} = \frac{0.9\lambda}{\beta\cos\theta}\,, \quad (3.2.1.4)$$

where $\mathrm{D_{crys}}$ is the average nanocrystallite size (nm), λ - is the X-ray wavelength (1.542 Å), β is the full-width at half-maximum (FWHM) intensity (in radians), and θ- is the half of the diffraction peak angle.

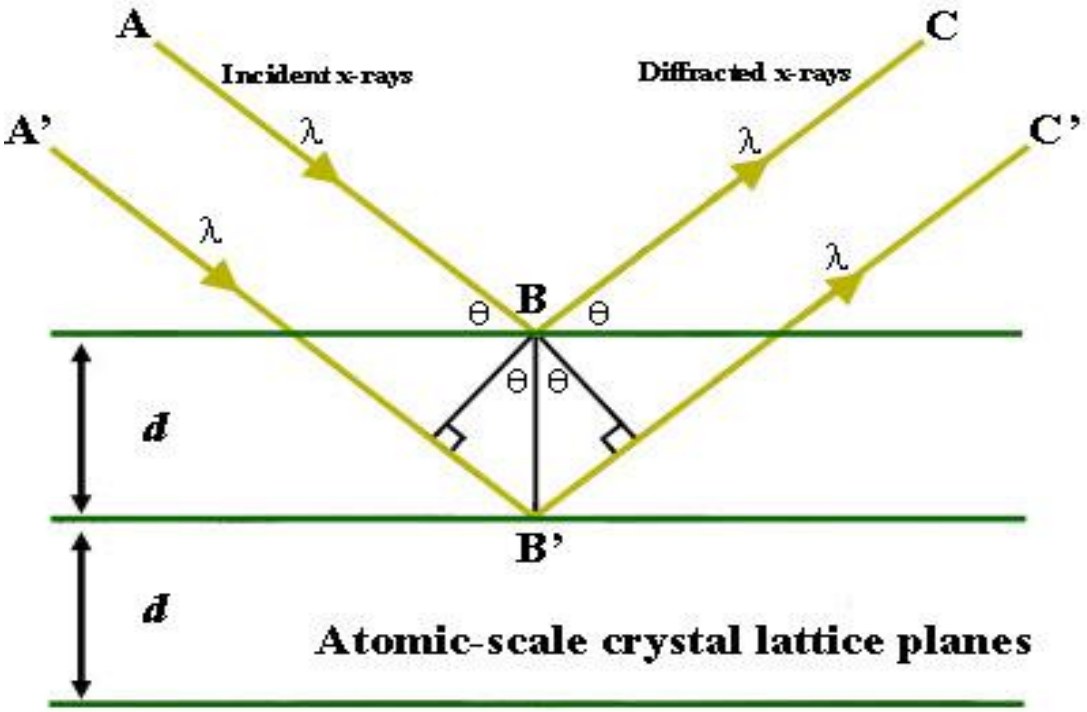

Figure 3.2: Geometry behind Bragg scattering. [85]

3.2.2 Raman spectroscopy (RS

Raman spectroscopy is used in condensed matter physics and chemistry to study vibrational, rotational, and other low-frequency modes in a system. It relies on inelastic scattering, or Raman scattering of monochromatic light, commonly from a laser. The laser light interacts with phonons or other excitations in the system, resulting in the energy of the laser photons being shifted up or down. The shift in energy gives evidence about the phonon modes in the system. The energy level diagram for Raman scattering is shown in figure 3.3 [86].

Infrared spectroscopy yields similar information, but complementary evidence. For a molecule to exhibit a Raman Effect, an alteration in polarizability or the amount of deformation of the electron cloud with respect to the vibrational coordinate, is necessary. The amount of the polarizability change will regulate the Raman scattering intensity [87], nevertheless the Raman shift is equal to the vibrational level that is involved. Raman spectroscopy is normally used in chemistry, since vibrational information is very specific for the chemical bonds in molecules [88].

In solid state physics, Raman spectroscopy is used to, amongst other things, characterize materials and find the crystallographic orientation of a sample [89]. In this study the samples were analyzed using a Jobin Yvon T64000 Raman spectrometer equipped with a liquid nitrogen cooled CCD detector. Signal was excited in a backscattering geometry using the 514.5 nm argon ion laser line. The sample was mounted in a room temperature cell used in conjunction with a Raman microscope. The power at the sample varied between 0.2 and 0.5 mW with the beam focused to an area of approximately 5-10 microns in diameter. All the Spectra were recorded at room temperature (295K). The experimental set-up is shown in figure: 3.4.

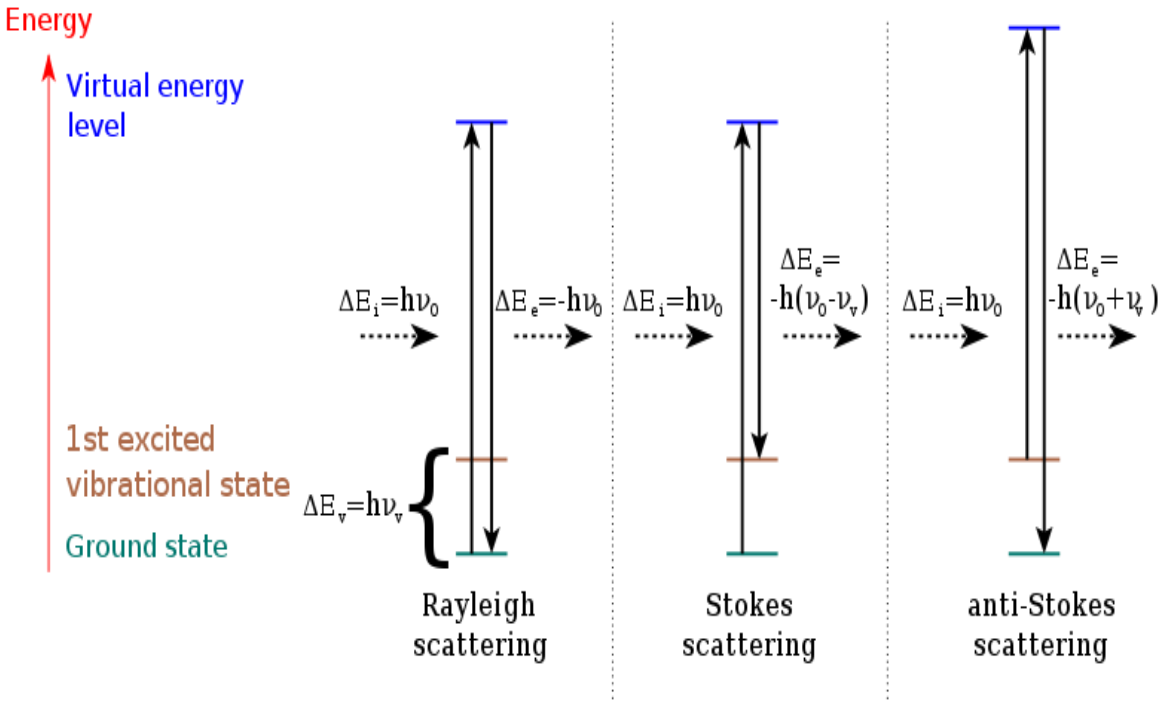

Figure 3.3: The different possibilities of light scattering showing Rayleigh scattering (no exchange of energy: incident and scattered photons have the same energy), Stokes Raman scattering (atom or molecule absorbs energy: scattered photon has less energy than the incident photon) and anti-Stokes Raman scattering (atom or molecule loses energy: scattered photon has more energy than the incident photon) [88]

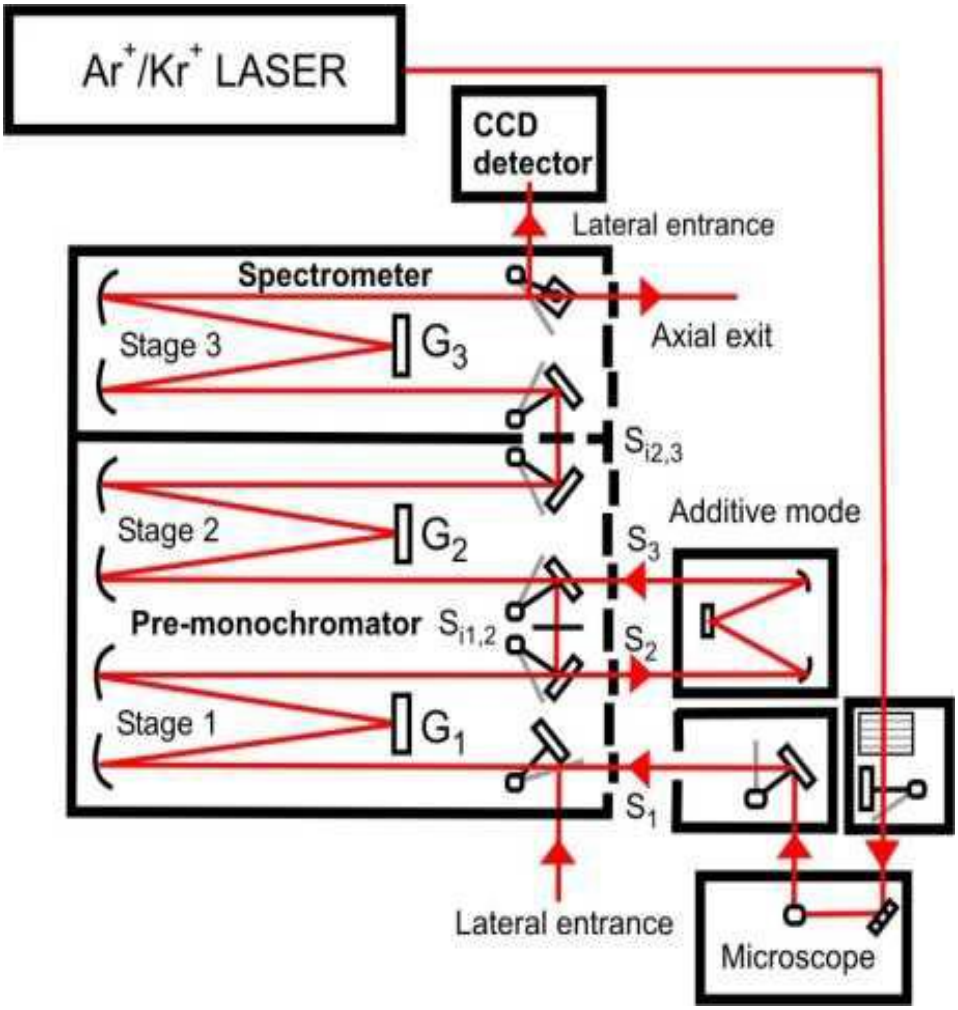

Figure 3.4: Optical diagram of JYT64000 monochro-mator in a triple additive and subtractive mode. [90]

3.2.3 Scanning Electron Microscope (SEM) and SEM Energy Dispersive X-ray (EDX) Spectroscopy

Scanning electron microscope (SEM) is a microscope that uses a beam of electrons to illuminate a specimen and create an enlarged image, which provides the surface and internal information on a nanometer scale. Electron microscopes have much greater resolving power than light microscopes, and can obtain much higher magnifications [91].

The electron microscope is extensively used for inspection, quality assurance and failure analysis applications in industry, particularly for microelectronic device fabrication. SEM has made crucial contributions to science and engineering, and made them essential tools in nanotechnology for analyzing nanostructures.
Schematic interactions of a specimen with incident electrons are illustrated in figure 3.5 [92].

Manfred von Ardenne pioneered the Scanning Electron Microscope (SEM) and built his universal electron microscope in the 1930s. In the SEM, a very fine beam of electrons with energies up to several tens KeV is focused on the surface of a specimen, and is scanned across it in a parallel pattern. The intensity of emission of secondary and backscattered electrons is very sensitive to the angle at which the electron beam strikes the surface of the sample.

The emitted electron current is collected and amplified. The magnification produced by the SEM is the ratio between the dimension of the final image displayed and the scanning field on the specimen [93]. Usually, the magnification range of the SEM is between 10 to 222,000 times, and the resolution is between 4 - 10 nm.

Generally, the Transmission Electron Microscopy (TEM) resolution is about an order of magnitude greater than the SEM resolution, however, because the SEM image relies on surface processes rather than transmission, it is able to

image bulk samples and has a much greater depth of view, and so can produce images that are a good representation of the overall 3D structure of the sample. SEM images of semiconductors materials are usually conductive or semi-conductive that could be as a result of external disturbances such as a stray magnetic field, mechanical vibrations, etc [94]. Often disturbances in SEM images are caused by structural or installation conditions such as:

- Leakage: Magnet field from distribution board High-tension line located too close to the instrument
- Low floor strength
- Improper grounding.

A common preparation technique is to coat the sample with a several-nanometer layer of conductive material, such as carbon from a sputtering machine. However during coating process a slight damage on the samples can result. It should also be pointed out that the specimen might be damaged by the electron-beam focused for a long time on a small spot.

SEM measurements were conducted to define the size and morphology of synthesized doped and undoped TiO_2 nanomaterials using a SmartSEM40® V05.03XB operating software for NEON® and 15xx crossBeam® FIB workstation with Gemin® FESEM column. The elemental composition was estimated using Energy Dispersive spectrometer (EDS) which was carried out using a JEOL–JEM 1200EXII which has an EDAX detector. The samples were tilted 45 °C in situ in the microscope to perform the analysis.

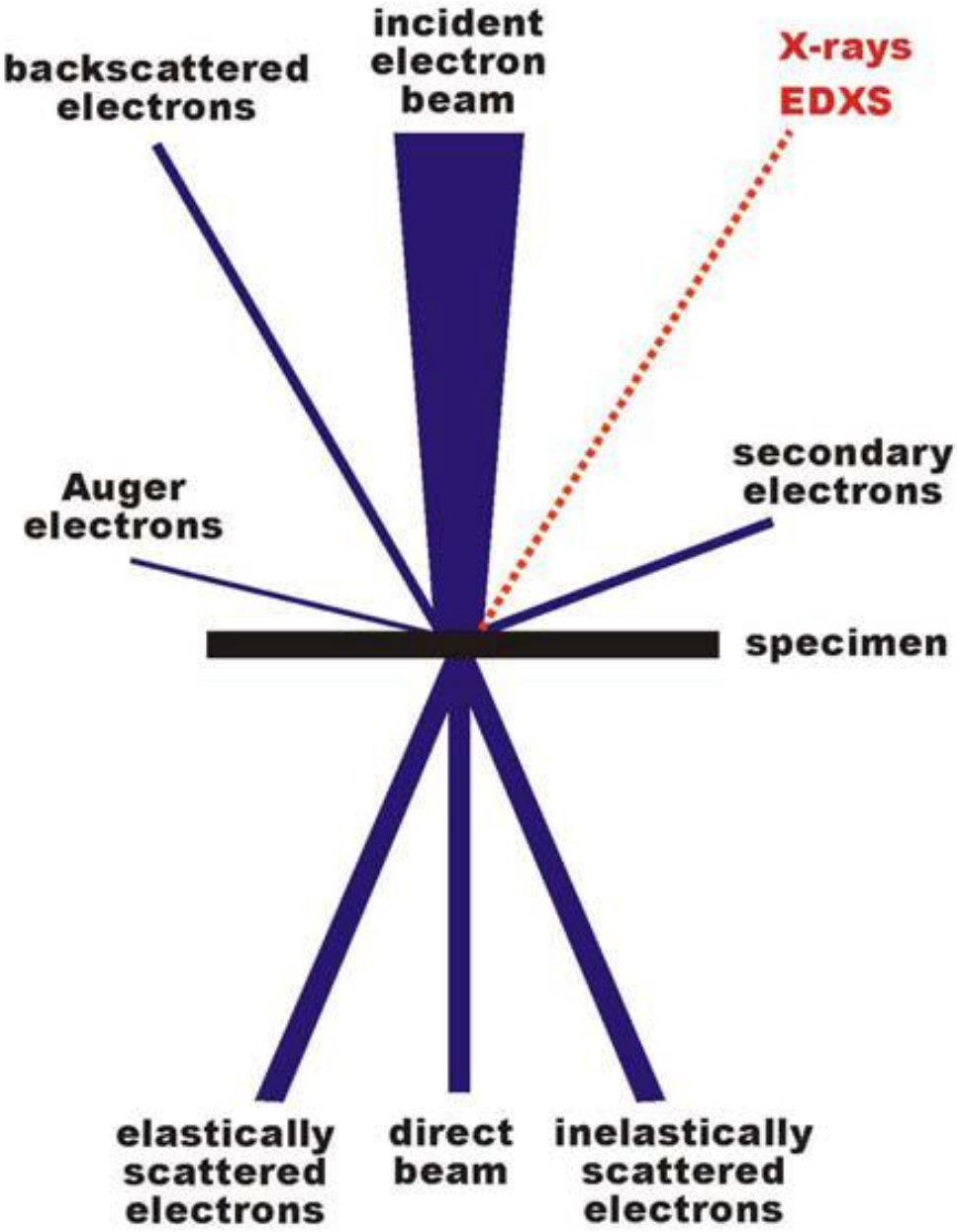

Figure 3.5: Scheme of electron-matter interactions arising from the impact of an electron beam onto a specimen. A signal below the specimen is only observable if the thickness is small enough to allow some electrons to pass through. [95]

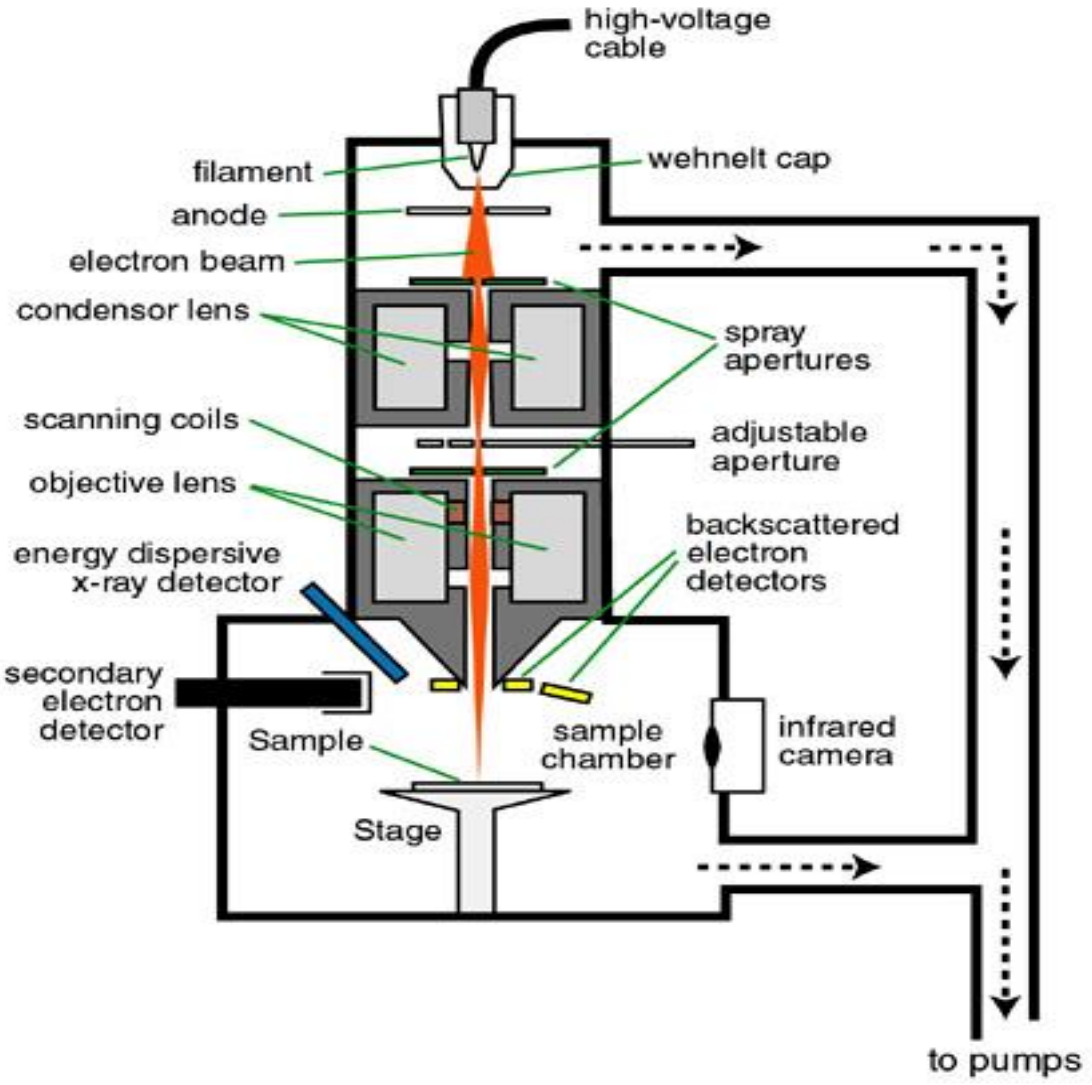

Figure 3.6: Scanning Electron Microscope overview. [96]

3.2.4 Diffuse Reflectance Spectroscopy (DRS)

Many molecules absorb ultraviolet (UV) or visible light. The absorption of UV or visible radiation is caused by the excitation of outer electrons, from their ground state to an excited state. The Bouguer-Lambert-Beer law forms the mathematical and physical basis for the light absorption measurements on gasses and in solutions [97]. According to this law, absorbance is directly proportional to the path length, l, and the concentration of the absorbing substance, *c*, and can be expressed as:

$$A = \varepsilon l c \qquad (3.2.4.1)$$

where ε is a constant of proportionality, called the absorptivity. In addition, absorption strongly depends on the types of samples, and the environment of the sample. For instance, molecules absorb radiation of various wavelengths depending on the structural groups present within the molecules, and show a number of absorption bands in the absorption spectrum. The solvent in which the absorbing species is dissolved also has an effect on the spectrum of the species [98].

Additionally, the size of the particle is also essential. If the size of the particle d»λ, light interacts with the samples instead of absorption, with parts of the light scattered and reflected. When we are dealing with solid samples (Figure 3.7), light penetrates into the sample; undergoes numerous reflections, refractions, diffraction and emerges finally diffusely at the surface.

The Bouguer-Lambert-Beer law cannot handle solid samples, which is based on the assumption that the light intensity is not lost by scattering and reflection processes [99]. The diagram shown in figure 3.7 illustrates the schematic view of DRS accessories and two components of reflection as the incoming light interact with the sample.

Diffuse reflectance measurements are commonly analyzed based on the Kubelka-Munk equation:

$$F(R_\infty) = \frac{k}{s} = \frac{1-R^2}{2R} \qquad (3.2.4.2)$$

where k and s are absorption and scattering coefficients respectively, and R is the reflectance at the front face. F (R∞) is termed the Kubelka-Munk function and is proportional to the concentration of the adsorbate molecules. From the onset of the plot of Kubelka-Munk function vs wavelength or photoenergy, the band gap energy of a semiconductor can be easily calculated [100]. However, to measure a diffuse reflectance spectrum, the diffusely reflected light must be collected with an incorporated sphere, avoiding secularly reflected light and using a reference standard such a white standard.

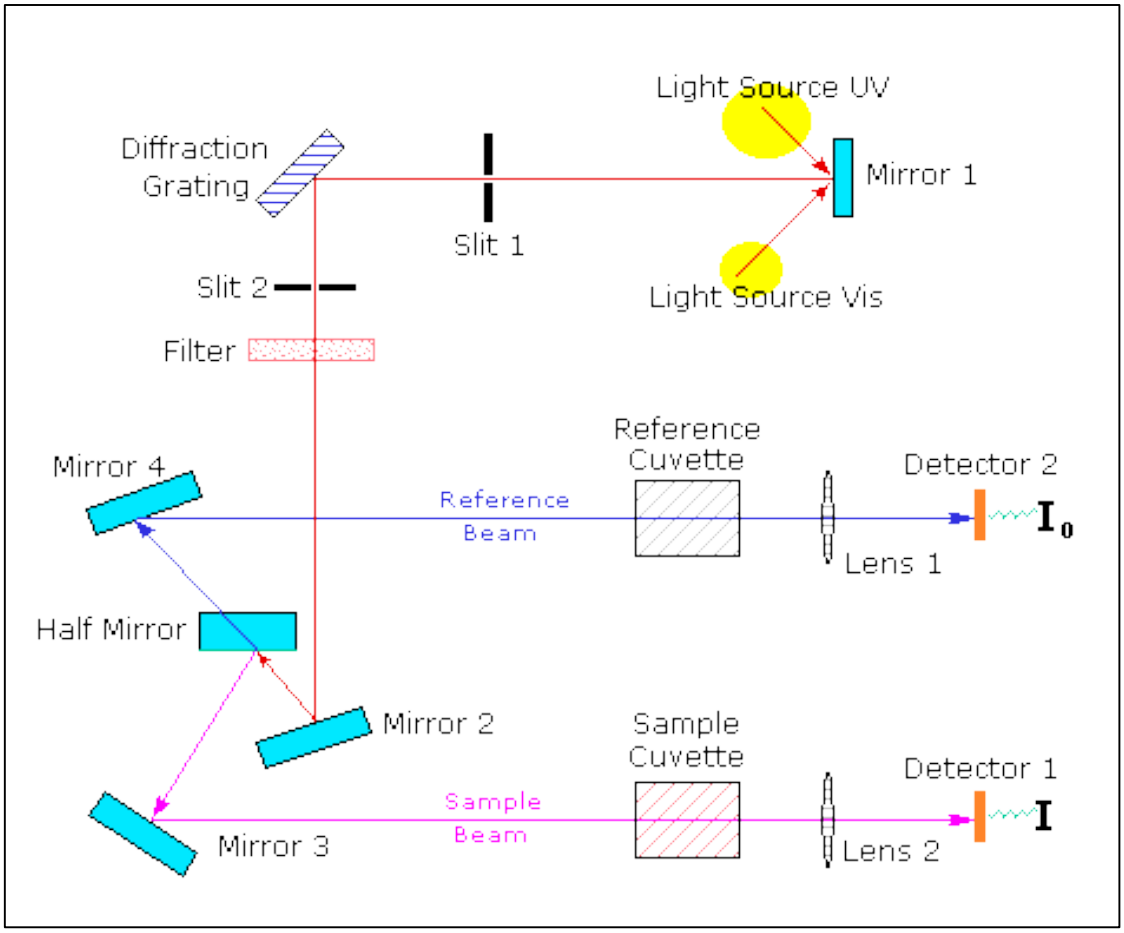

Figure 3.7: A schematic view of the external DRS. [101]

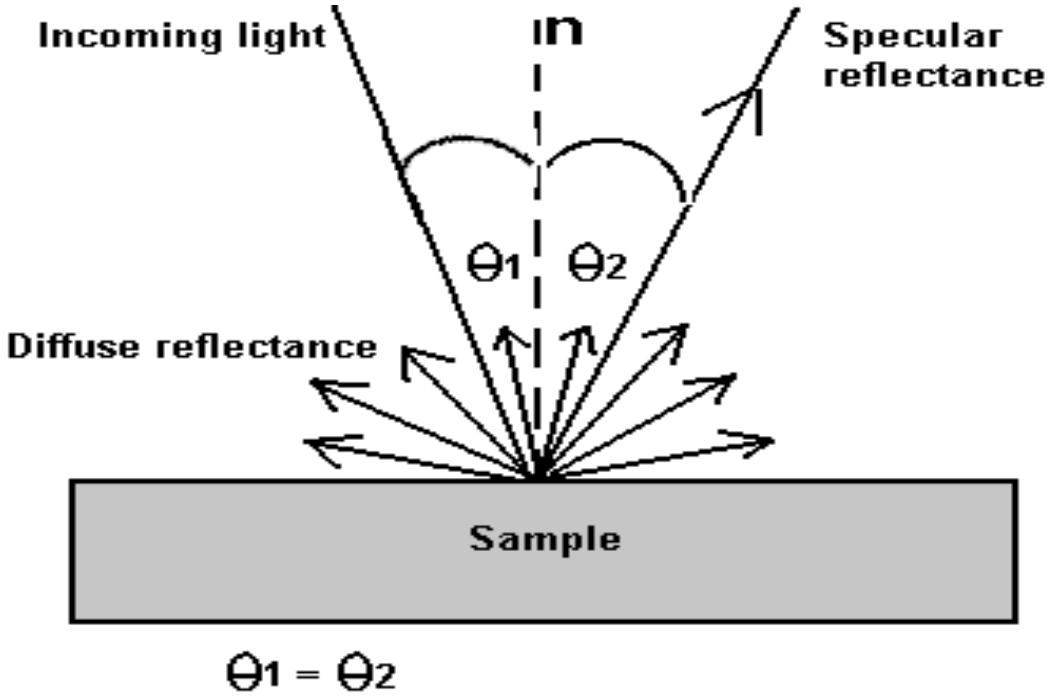

Figure 3.8: The two components of reflection: specular and diffuse reflection; represents the surface normal, an imaginary line at 90° to the sample surface. [101]

CHAPTER 4

RESULTS AND DISCUSSION

In this chapter the x-ray powder diffraction (XRD), Raman spectroscopy (RS), Scanning Electron Microscopy (SEM) and Diffuse Reflectance Spectroscopy (DRS) results will be presented. For XRD the focus will be on phase identification, phase transformations, grain size estimations from Scherer's equation and lattice parameters calculations using Brag laws. The effects of metal dopants on the structural and optical properties studied using the techniques mentioned above as well as the locations of metals will also be presented and discussed.

4.1 XRD RESULTS

4.1.1 Pure-TiO_2

It is now well established that for pure TiO_2 the X-ray spectra display the most intense anatase peaks at 2Θ = 25.28° and 37.7° corresponding to (101) and (004) planes respectively; for the rutile phase around at 2Θ = 27.7°, 37.3° and 55.1° corresponding to (110), (101) and (211) planes, respectively [102, 103] and for brookite at 2Θ = 25.34° and 25.69° corresponding respectively to the planes (120) and (111) as outlined by Di Paola *et al*. in (2008) [102]. Further confirmation of these observations was by Moret *et al.* (2000) [104], who reported that the brookite diffractogram reflects distinctive peaks at 2θ = 25.3°, 25,7°, 30.8° and 36.2°.

Figure 4.1 shows the X-ray diffraction (XRD) spectra of the four samples annealed at different temperatures in the 2-theta range from 10 to 90˚. In this range, for the pure TiO_2 as prepared sample, no anatase or rutile peaks were observed and this indicates that the sample is mostly amorphous. For the sample preheated at 300 ^oC, peaks associated with the anatase phase are

observed which indicates that with standard sol-gel method, the initial TiO_2 phase is anatase.

These peaks intensify as the calcination temperature is increased to 600 °C suggesting that there is a growth in the particle size of TiO_2. At this temperature, the anatase peaks are still the only peaks observed, which is an indication that transformation temperature has not yet been reached. At 900 ^oC, all the anatase peaks have disappeared and only the rutile peaks are observed. This indicates that the sample has completely transformed from anatase to rutile between 600 and 900 °C. This work agrees very well with previous report by Francisco *et al.* in (2002) [105] that anatase to rutile transformation occurs around 700 ^oC.

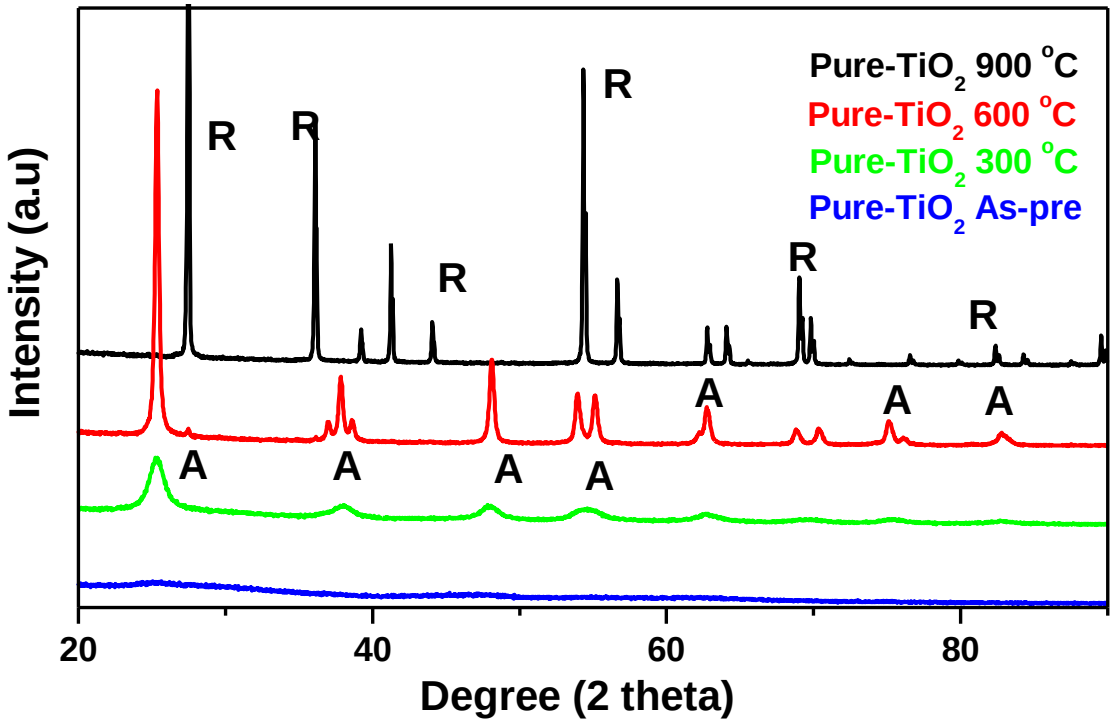

Figure 4.1: X-ray diffraction spectra of the pure- TiO_2 powder before and after annealing at different temperatures. A and R represents anatase and rutile phases, respectively.

4.1.2 5% Au-TiO_2

Figure 4.2 shows the XRD spectra of 5% Au-TiO_2 which was prepared at room temperature then annealed at various temperatures afterwards. The as-prepared sample of Au-TiO_2 was found to be of amorphous phase. The interesting feature in this XRD profile is that the reflections at 2θ = 38°, 44°, 65° and 78° associated with Au metal are also observed. Similar Au metal peaks were also observed by Cheng *et al.* in (2010) [106] who also found peaks at 38.1°, 44.4°, 64.6°, and 77.5° associated with the (111), (200), (220), and (311) reflections of the Au core. In all samples, the spectra exhibited similar Au peaks, indicating that no phase change occurred for Au during annealing processes.

At 300 ºC, peaks associated with anatase phase start to appear with the most intense one observed at 2θ = 25°. The intensities of both the anatase and Au peaks increase considerably as the temperature increases as can be seen for the profiles of samples annealed at 600 and 900 °C. At 600 °C, there are no peaks associated with rutile phase whereas at 900 °C anatase disappeared completely and only the rutile peaks are present. This indicates that Au does not affect the anatase to rutile transformation temperature. The fact that Au peaks are observed at all temperatures indicates that gold does not enter the TiO_2 matrix hence is probably on the surface of the material.

Debeila *et al*. in (2005) [107] studied the unit cell volume of Au-TiO_2 complex for both anatase and rutile and found out that they were similar to those of pure TiO_2 and from this observation it was suggested that gold has no effect on TiO_2 matrix which is consistent with what is found in this study. It was also noted by Debeila *et al*. (2005) that the phase transformation of Au-TiO_2 occurs around 700 °C which agrees with the present work. The phase transformation temperature was also confirmed by Uddin *et al.* in (2008) [108].

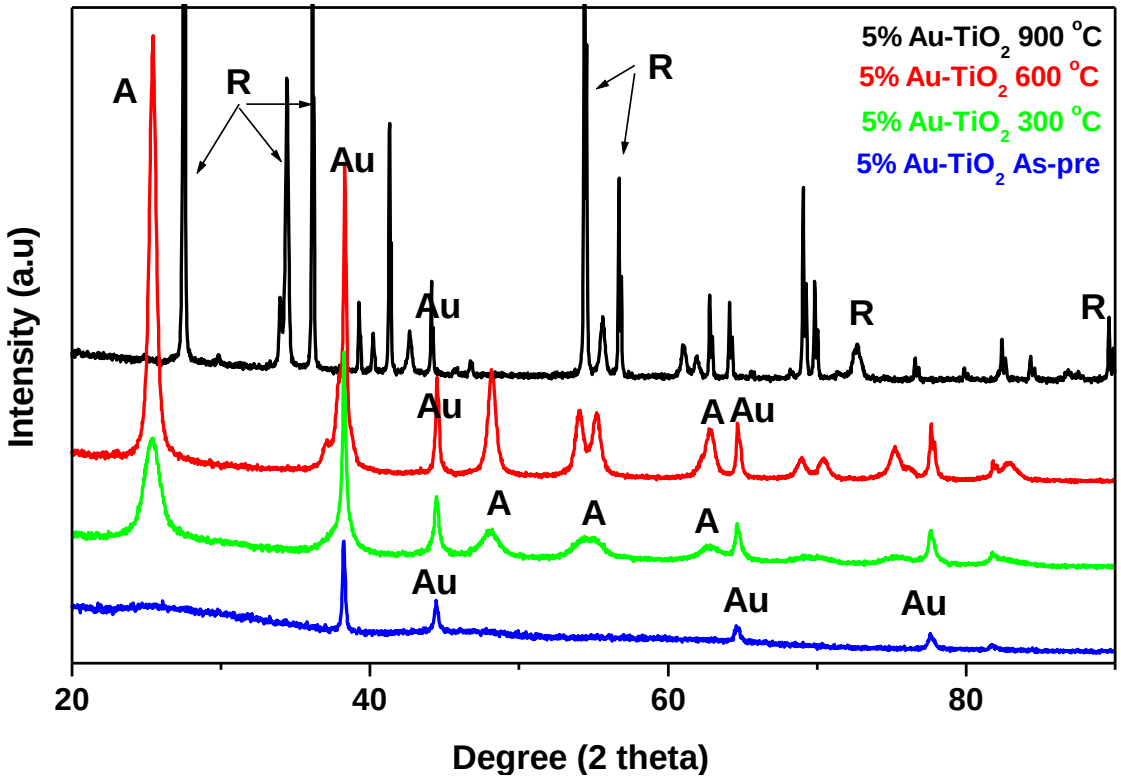

Figure 4.2: X-ray diffraction spectra of the Au- TiO_2 powder before and after annealing at different temperatures. A and R represents anatase and rutile phases, respectively

4.1.3 5% Pd-TiO_2

Figure 4.3 shows the XRD spectra of nano-sized 5% Pd-TiO_2 samples annealed at different temperatures. Unlike the Au doped TiO_2, the as-prepared Pd doped sample exhibited the characteristic peaks of the anatase titania at 2θ = 25° (major), 37°, 48°, 55°, 56° and 62°. The XRD spectra of the sample heated at 300 ^oC is similar to the as prepared except that a small peak associated with PdO starts to appear. At 600 °C, the XRD profile shows a combination of anatase and rutile phases which indicates that transformation has already started to occur.

At 900 °C, only the rutile titanium oxide phase is observed. This results show that Pd affects the transformation temperature by reducing it. It is worth noting that at 300 °C, peaks associated with PdO are observed at 2θ = 30.3°. As the temperature is raised to 600 °C another PdO peak and Pd peak start to appear at about 34.1° and 68° respectively. This agrees very well with the experimental observation by Datye *et al*. in (2000) [109] during the group's investigation of AlO_3 doped with (5%Pd) where they found peaks associated with PdO and Pd around 2θ = 34.1° and 40.4°, respectively.

This indicates that the effectiveness of Pd as an oxidation catalyst depends more on its complex interactions with oxygen gas molecules (O_2) to form surface PdO which reacts in a Mars–van Krevelan redox mechanism during catalytic oxidation at temperatures below 600 ^oC. For the sample heated at 900 ^oC, PdO peaks disappear completely while new peaks start to appear at 40, 47.1 and 68.1 degrees 2θ which can be attributed to the presence of metallic palladium which was also noted by Chen *et al.* (2005) [110] during their palladium (Pd) optical properties study.

This shows that PdO reduces to metallic Pd at high temperatures as suggested by Suhonen *et al*. in (2001) [111]. Datye *et al*. in (2000) [109] reported that PdO experiences complete reduction and reduces to metallic Pd at temperatures above 700 ◦C under normal atmospheric pressures. This is in good agreement with the present work. The results show that Pd is initially present as an oxide (PdO) and converts to metallic Pd at higher temperatures.

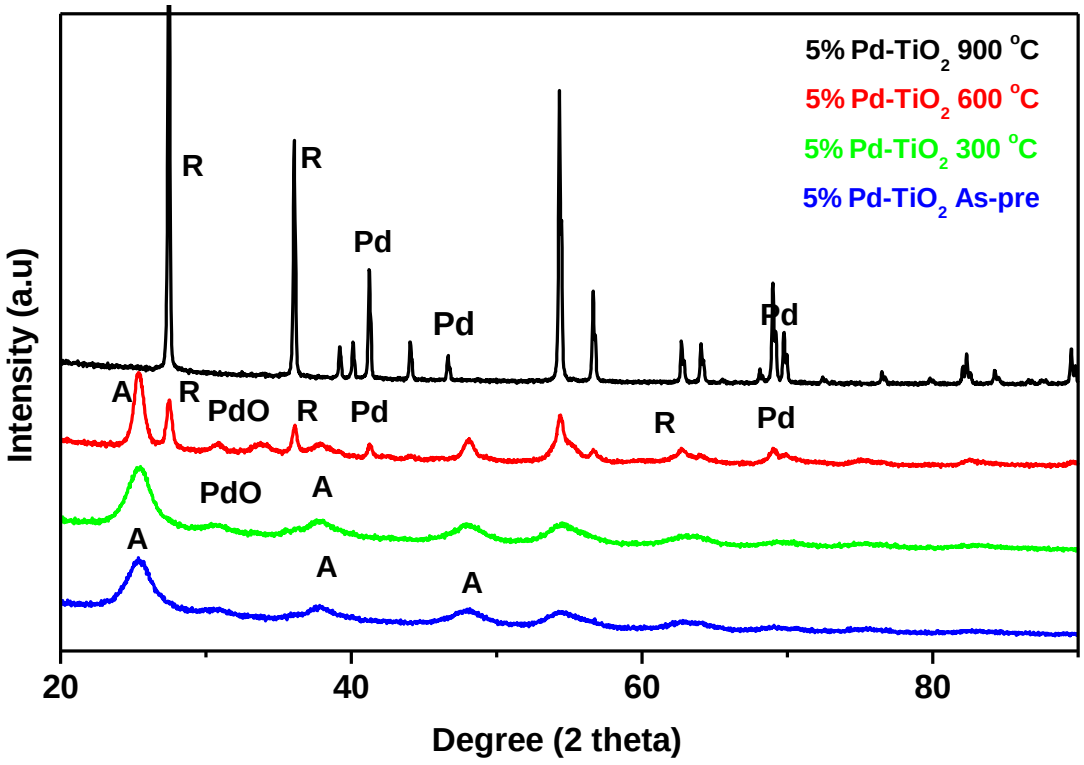

Figure 4.3: X-ray diffraction spectra of the 5% Pd- TiO_2 nano-powder before and after annealing at different temperatures. A and R represents anatase and rutile phases, respectively.

4.1.4 5% Ag-TiO_2

Figure 4.4 shows the X-ray spectra of 5% Ag-doped TiO_2 nano-powders calcined at 300, 600, 900 °C and as-prepared. The as-prepared and 300 °C samples consist of a single, less intense anatase peak at 2θ = 25°; which suggest that the material is mostly amorphous at low temperature. As the annealing temperature rises, the material shows a high degree of crystallinity and existence of fully intensive anatase phase which is indicated by peaks at 2θ = 25.9, 36.4, 48.2, 53.9, 62.5 and 74.9° similar to those reported by Hung *et al*. in (2008) [112].

Traces of AgO are observed at about 2θ = 32.2° and 82.9°, especially at 600 ^{0}C. At 900 °C rutile peaks at 2θ = 39.2°, 69.3° and 70.5 9° are evident and are in good agreement with the work reported by Raju *et al*. in (2009) [113]. At the same temperature, the profile shows silver peaks and no silver oxide peaks, which indicates that AgO at high temperatures reduces to metallic silver and suggest a homogeneous distribution of metallic Ag on the surface of the titania matrix since it can be detected with XRD. This observation suggests that at low temperatures silver is initially present as an oxide and converts to a metal at higher temperatures and this was also noted by Sen *et al*. in (2005) [114] and Feng *et al.* in (2011) [115].

It was also observed that the diffraction peaks corresponding to the rutile phase of TiO_2 are dominant with no traces of the anatase phase peaks observed for 900°C calcined sample indicating that TiO_2 has fully transformed into rutile [115]. However, because of a large difference in their ionic radii (Ti^{4+} = 74.5 pm and Ag^+ = 129 pm in octahedral coordination), the Ag^+ ions introduced by the sol–gel process are unable to enter the TiO_2 lattice to form a stable solid solution, rather they are dispersed between the anatase/rutile grains as suggested also by Mohamed and Al-Sharif in (2012) [116].

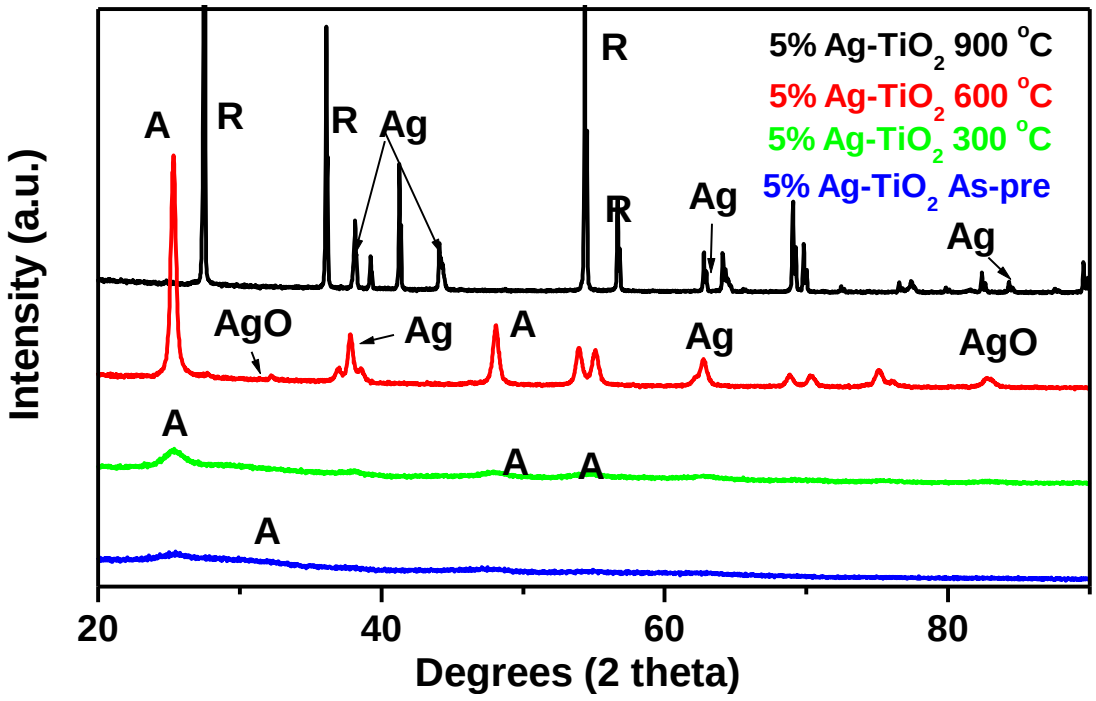

Figure 4.4: X-ray diffractograms for Ag-doped TiO_2 gel nano-powders annealed at different temperatures. A and R represents anatase and rutile phases, respectively.

4.1.5 5% Pt-TiO_2

The X-ray diffraction spectra for Pt/TiO_2 nano-particles prepared by a standard sol-gel route with a Pt dopant of 5% weight percentage are presented in figure 4.5, with samples heated at different temperatures of 300, 600 and 900 °C. At 300 ^oC, peaks associated with anatase phase start to appear. The XRD spectra of Pt-TiO_2 nano-sample heated at 300°C shows few less intensified peaks associated to anatase phase, with the main peak at $2\theta = 25^o$. At 600 °C a peak at $2\theta = 40°$ associated with metallic Pt is observed. At this temperature, one can also see the development of rutile peaks near $2\theta = 27°$, 54°, 64° and 69°. More peaks associated with Pt metals i.e. at $2\theta = 40°$, 45.7° and 62.6° are observed at 900 °C and are similar to those observed by Guo and Li in (2006) [117].

This work compares very well with the findings by Rosario and Pereira in (2014) [118] who reported that pure TiO_2 sample is composed only by anatase phase but in the presence of Pt, a small amount of rutile phase can be detected from the 600 °C annealed sample. This is also shown in table 4.1 of the present work. The work also agrees with the observations of Choi *et al*. in 2009 [119]. All these suggest that platinum doping has effect on phase transformation temperatures. It is worth noting that the peak at $2\theta = 40.1°$ cannot be observed on the 300 and 600 °C annealed samples, due to overlap from an anatase peak [120]. As seen from table 4.1, the presence of platinum has an effect on the anatase-to-rutile phase transition temperature. The transformation occurs earlier than 600°C, although it was not complete until 900 °C. Platinum has an effect on TiO_2 phase transformation although it does not restrict the growth of the nanocrystalline TiO_2 particles as detailed in table 4.1.

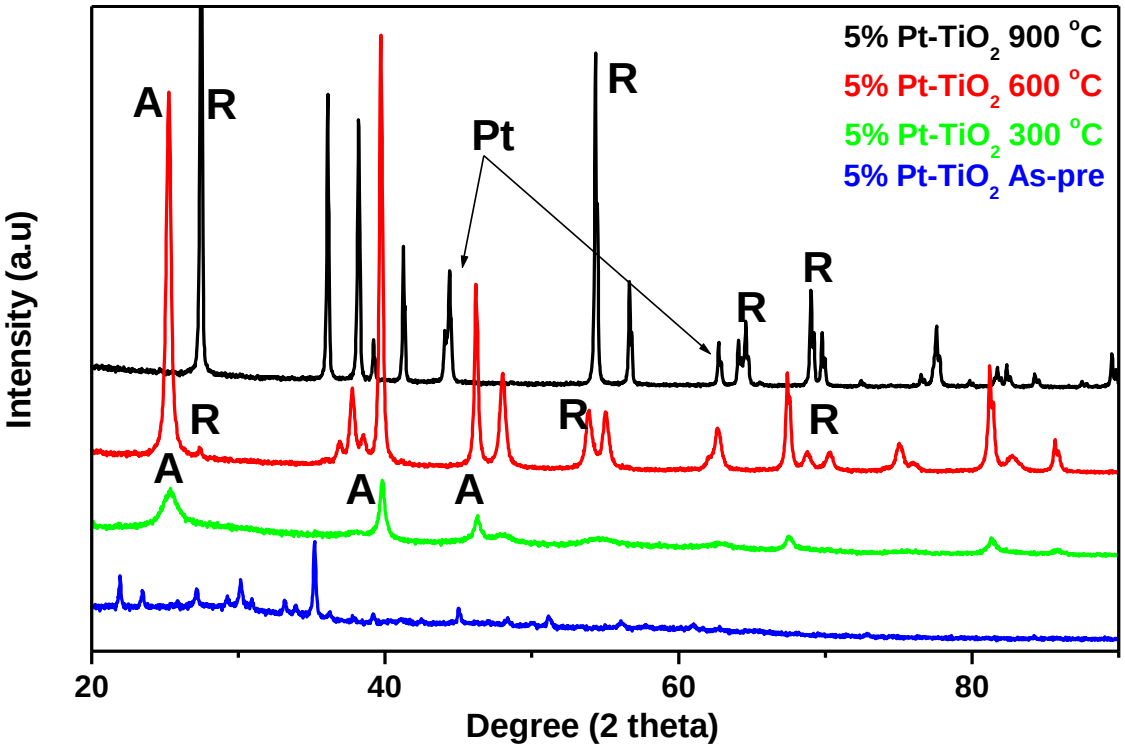

Figure 4.5: X-ray diffraction spectra of the Pt- TiO_2 nano-powder before and after annealing at different temperatures. A and R represents anatase and rutile phases, respectively.

4.1.6 Lattice Parameter Determination

The experimental lattice parameters of anatase and rutile with their respective cell volumes of metal loaded TiO_2, along with the lattice parameters of pure TiO_2 are shown in table 4.1. The X-ray diffraction peaks of crystal plane [101] at 2θ = 25° and [200] at 2θ = 48° for the anatase and [101] at 2θ = 36° and [200] at 2θ = 39° for the rutile were used to determine the lattice parameters of metal doped TiO_2. All lattice parameters calculated here were obtained using the following equations:

$$\frac{1}{d_{hlk}{}^2} = \frac{h^2}{a^2} + \frac{k^2}{b^2} + \frac{l^2}{c^2} \qquad (4.1.6.1)$$

where **a = b ≠ c;** which are the lattice parameters
and the Bragg's equation:

$$2d\mathrm{Sin}\theta = n\lambda \qquad (4.1.6.2)$$

The anatase and the rutile crystal phases for all metal loaded TiO_2, have almost the same lattice parameters as that of the pure TiO_2 and also well comparable with literature. This also indicates that the metals prefer the surface regions and not getting into the matrix.

Table 4.2 illustrates, the average particle sizes for metal loaded TiO_2 samples annealed at different temperatures (i.e As-prepared (100 ^{0}C), 300, 600 and 900 ^{0}C) along with the pure TiO_2 for comparison. Calculation of particle sizes were calculated using the Scherrer equation presented below:

$$D = \frac{K\lambda}{\beta cos\theta} \qquad (4.1.6.3)$$

With K being the dimensionless constant, θ being the Bragg angle, being the radiation wavelength and β being the full width at half-maximum.

For the 900 ^{0}C heated sample we observe that the presence of gold does not restrict the growth of the nanocrystalline TiO_2 particles although there is a slight reduction in grain growth for the samples heated at 100 and 300 ^{0}C. The presence of silver does restrict the growth of the nano crystalline TiO_2 particles

after heating at 600 ^{0}C. According to the calculated particle sizes detailed in table 4.2, the presence of platinum has an effect on the reduction of the crystalline growth after annealing at 600°C which indicates that it also has an effect on the anatase-to-rutile transformation temperature.

The 900°C platinum doped has a particle size reduction of 1.68%. As presented in table 4.2, palladium noticeably restricts the growth of the crystalline TiO_2 particles slightly for the as-prepared and 300°C samples for as much as 17.01% and 10.98% both in anatase phase. For the sample heated at 600°C it becomes clear for one to notice that we have both anatase and rutile, which is clear indication of the fact the phase transition happened at early temperatures. Heating to 900°C we observe total transformation to a rutile phase with a restriction in the grain size of 1.65%. Therefore we can conclude that platinum and palladium dopants do affect the anatase to rutile phase transformation.

Table 4.1: Lattice parameters of pure and metal loaded TiO_2

Sample	Calcination Temperature	Crystal Phase	Lattice Parameters			
			a (Å)	b (Å)	c (Å)	Unit cell Volume ($Å^3$)
Anatase [121]		Anatase	**3.784**	**3.784**	**9.515**	**136.238**
Rutile [121]		Rutile	**4.593**	**4.593**	**2.959**	**62.422**
Undoped TiO_2	300 ℃	Anatase	3.7828	3.7828	9.4395	135.0718
	600 ℃	Anatase	3.7828	3.7828	9.5275	136.3306
	900 ℃	Rutile	4.5837	4.5837	2.9666	62.3280
TiO_2 (5% Au)	300 ℃	Anatase	3.7807	3.7807	9.7383	139.1952
	600 ℃	Anatase	3.7719	3.7719	9.8924	140.7419
	900 ℃	Rutile	4.5720	4.5720	2.9706	62.9639
TiO_2 (5% Ag)	300 ℃	Anatase	3.7781	3.7781	9.4566	134.9864
	600 ℃	Anatase	3.7812	3.7812	9.5064	135.9149
	900 ℃	Rutile	4.5888	4.5888	2.9588	62.3033
TiO_2 (5% Pd)	100 ℃	Anatase	3.7847	3.7847	9.2844	132.9910
	300 ℃	Anatase	3.7754	3.7754	9.7170	138.5005
	600 ℃	Anatase	3.7754	3.7754	9.7170	138.5005
	600 ℃	Rutile	4.5968	4.5968	2.9363	62.0457
	900 ℃	Rutile	4.5968	4.5968	2.9480	62.2922
TiO_2 (5% Pt)	300 ℃	Anatase	3.7803	3.7803	9.2402	132.0510
	600 ℃	Anatase	3.7695	3.7695	9.9960	142.0315
		Rutile	4.6741	4.6741	2.9647	64.7699
	900 ℃	Rutile	4.5907	4.5907	2.9651	62.4863

Table 4.2: Average particle sizes for pure TiO_2 and Noble metals doped TiO_2 after heating for 1 hour at different temperatures.

TEMPERATURE (°C)	PURE TiO_2		5% Au-TiO_2		5% Ag-TiO_2	
	Size (nm)	**Phase**	**Size (nm)**	**Phase**	**Size (nm)**	**Phase**
As-Prepared (100 °C)	5.981619671	Anatase	5.405621521	Anatase	5.101815487	Anatase
300 °C	7.800688774	Anatase	7.583333046	Anatase	5.646436446	Anatase
600 °C	28.88303779	Anatase	16.91313801	Anatase	20.49734501	Anatase
900 °C	68.61039248	Rutile	71.13067384	Rutile	95.05011318	Rutile
TEMPERATURE (°C)	**PURE TiO_2**		**5% Pt-TiO_2**		**5% Pd-TiO_2**	
	Size (nm)	**Phase**	**Size (nm)**	**Phase**	**Size (nm)**	**Phase**
As-Prepared (100 °C)	5.981619671	Anatase	5.86027375	Anatase	4.964274875	Anatase
300 °C	7.800688774	Anatase	6.944063099	Anatase	4.934496567	Anatase
600 °C	28.88303779	Anatase	23.60165323	Anatase	11.34992068	Anatase
			31.40731709	Rutile	23.45086794	Rutile
900 °C	68.61039248	Rutile	67.47942952	Rutile	57.3052622	Rutile

4.2 RAMAN RESULTS

In this section, the results of the Raman studies, carried out to confirm the phase transformation, crystallinity and possible defects, are presented. Focus will be on the Raman spectra of anatase and rutile phases since brookite phase is highly unstable. The investigation of how each individual dopant will affect the Raman bands and phase transformation is illustrated within this section.

4.2.1 Raman results of undoped-TiO_2

According to group theory analysis, anatase has six Raman active modes (A1g + 2B1g + 3Eg). The Raman spectrum of an anatase single crystal has been investigated by T. Ohsaka in (1980) [122] and showed that the six allowed modes appear at 144 cm-1 (Eg), 197 cm-1 (Eg), 399 cm-1 (B1g), 513 cm-1 (A1g), 519 cm-1 (B1g), and 639 cm-1 (Eg) . The Raman spectra of rutile single crystal were investigated by Porto et al (1967) and detected the four Raman active modes at 143 (B1g), 447 (Eg), 612 (A1g) and 826 (B2g).

The Raman spectra of the undoped and annealed nanophase TiO_2 are shown in Figure 4.6. The samples annealed at 300 and 600 °C display a well resolved Raman peak at 153 cm^{-1} and three broader features in the high frequency region located at 399, 518 and 636 cm^{-1} associated with the anatase phase except that for the as-prepared sample the spectrum shows that the sample is mostly amorphous. The variations of the Raman peak positions of single and nanocrystalline samples are due to the effect of smaller particle size on the force constants [123].

For the sample calcined at 900 °C, three vibration peaks associated with the rutile phase around 612, 448 and 144 cm-1 (weak) are observed. No anatase peaks were observed at this temperature. In addition to the rutile peaks, a strong broad band at 238 cm-1 is observed. This band cannot be assigned to the fundamental modes allowed by symmetry in the rutile phase. Balachandran and Eror [124] explained its origin in terms of second-order scattering caused by a multiphonon process. This Raman result compliments very well the XRD

result for the undoped nanophase TiO_2 in that transformation occurs between 600 and 900 °C.

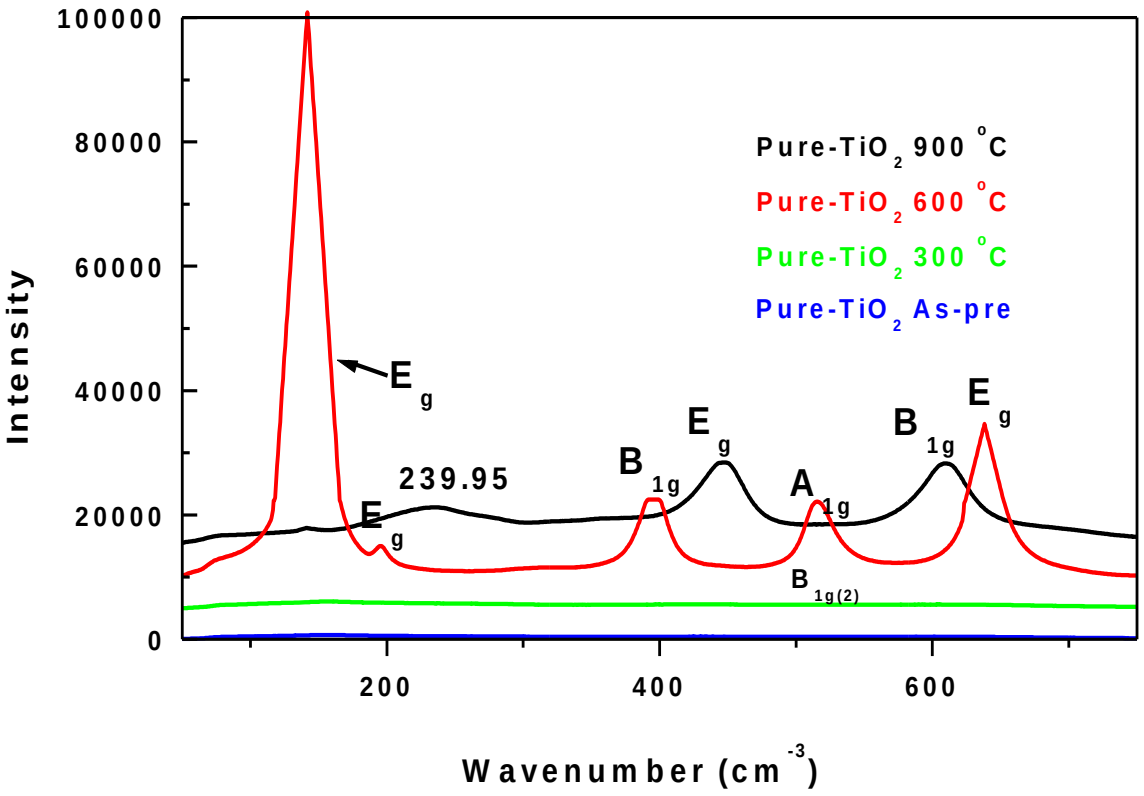

Figure 4.6: Raman Spectra of undoped-TiO_2 annealed at 300, 600, and 900 °C temperatures.

4.2.2 Raman Scattering Results of metal loaded-TiO_2

The Raman spectra of 5% Au-TiO_2 (similar for Ag doped) and 5% Pt-TiO_2 (similar for Pd doped) are shown in figures 4.7 and 4.8, respectively. The zoomed high frequency Raman spectra are shown in figures 4.9 and 4.10, respectively. The sharpness of the Raman peaks and the intensity signifies that the sample is highly crystalline. The low frequency Raman modes show a well resolved peak at around 153 cm^{-1}, and three broader features in the high frequency region located at around 399, 518 and 636 cm^{-1} associated with the E_g, B_{1g}, A_{1g} and E_g vibrational modes of the anatase phase, respectively.

The rutile phase is evident in samples annealed at 900 ^oC with peaks observed at 143 (weak), 446 and 610 cm^{-1} as expected [125] . Like with the undoped sample, the strong broad band at 238 cm^{-1} is also observed here along with the rutile peaks which cannot be associated with the rutile phase.

The rutile peaks are also observable for samples annealed at 600 ^oC 5% Pt and 5% Pd doped samples indicating that transformation starts earlier in these samples.The results agree well with the XRD results in that Ag and Au do not affect the transformation temperature whereas Pd and Pt do affect the anatase to rutile phase transformation.

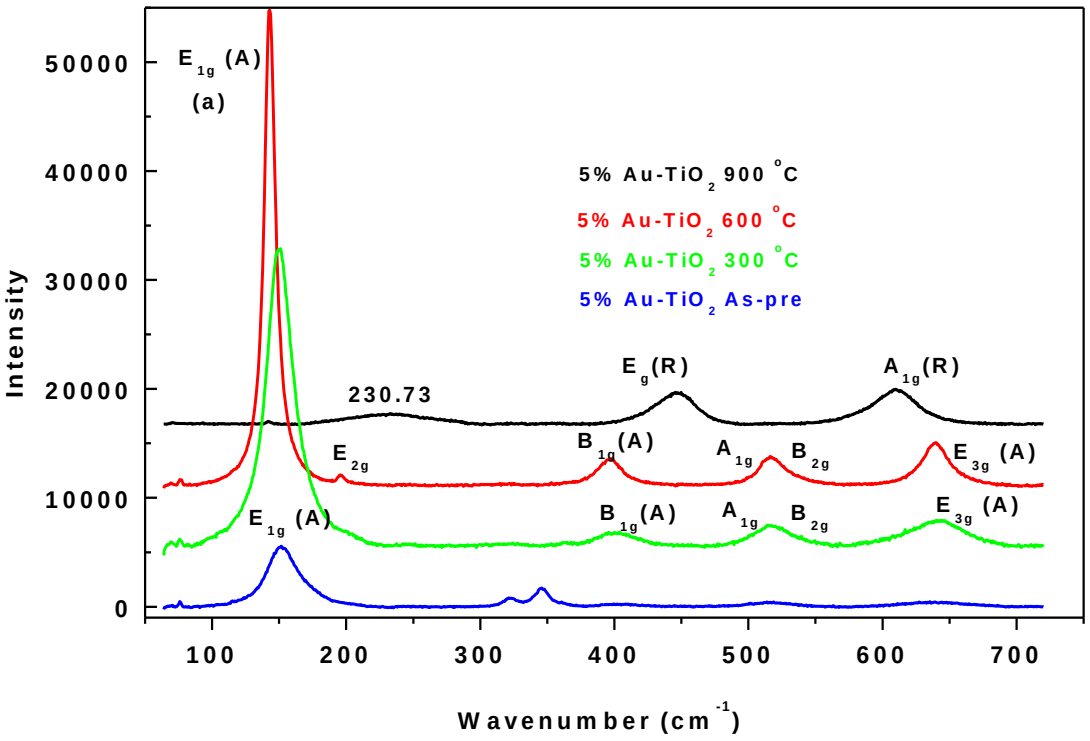

Figure 4.7: Raman Spectra of 5% Au-TiO_2 annealed at 300, 600, and 900 °C temperatures. A denotes anatase and R denotes rutile phase.

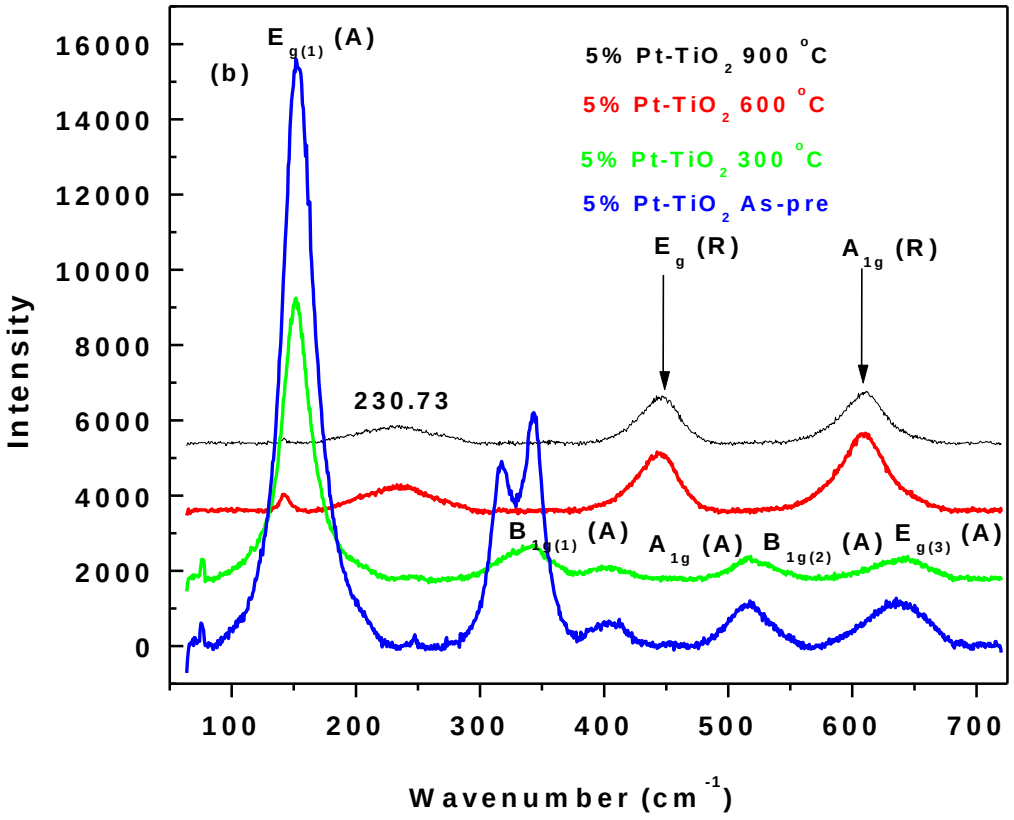

Figure 4.8: Raman spectra of 5% Pt-TiO_2 annealed at 300, 600, and 900 °C temperatures. A denotes anatase and R denotes rutile phase.

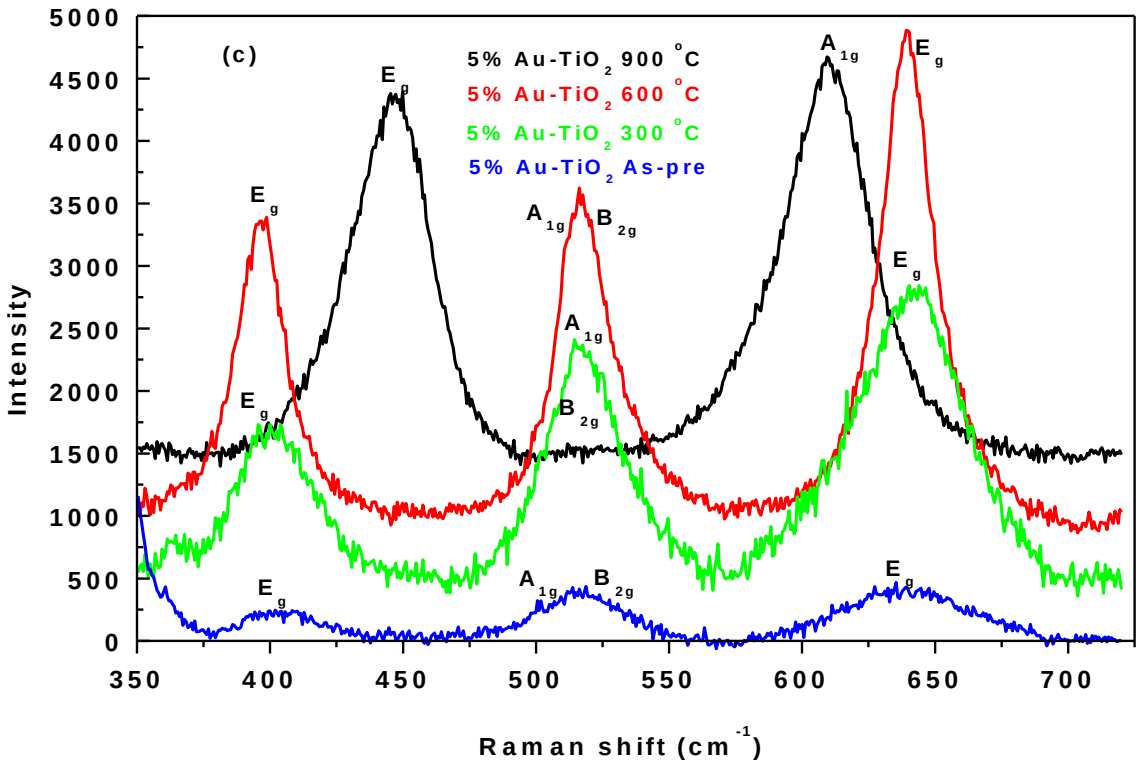

Figure 4.9: High frequency Raman spectra of 5% Au-TiO_2.

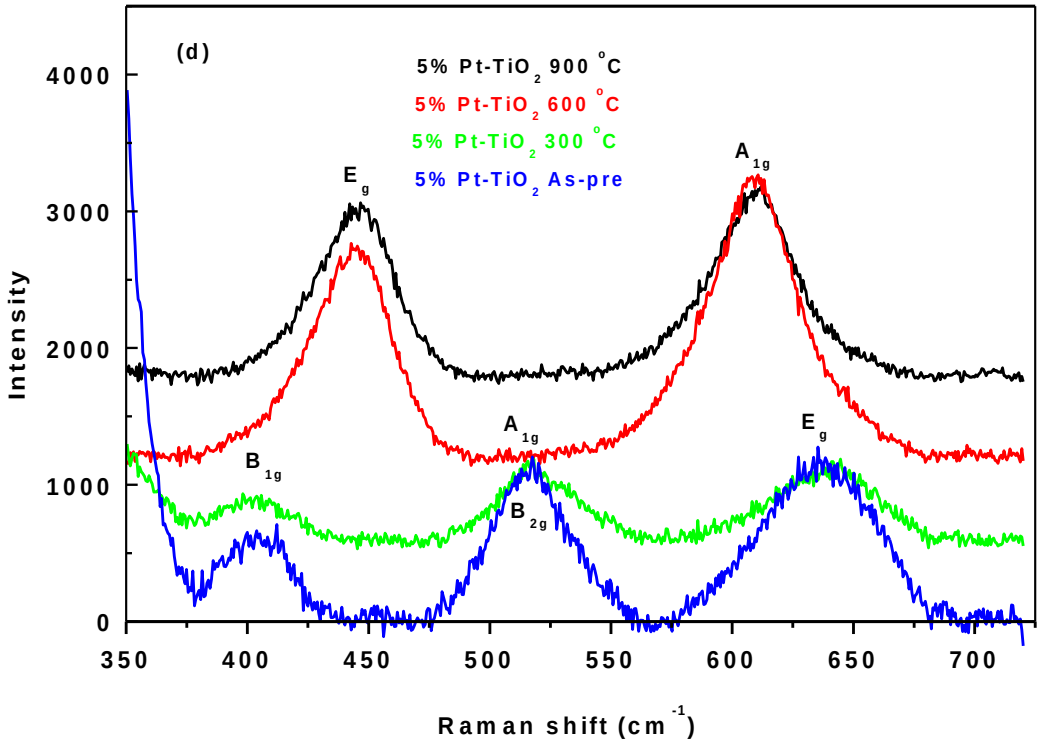

Figure 4.10: High frequency Raman spectra of nanophase 5% Pt-TiO_2.

4.3 SCANNING ELECTRON MICROSCOPY (SEM) RESULTS

The set of SEM micrographs for pure, 5% Au-doped, 5% Ag-doped and 5% Pt-doped samples (similar to 5% Pd-doped) are shown in figures 4.11, 4.12, 4.13 and 4.14, respectively. The figures typify what was observed for the sample species at the anatase and rutile phases; and that all samples have a porous network arrangement formed by enormous number of small spheres. The images show agglomeration of fairly spherically-shaped particular crystalline structure for all samples at 600 and 900 °C annealing temperatures although experienced a lot of charging in certain images. This SEM disorder can be caused by the following factors or conditions below:

- If the material is unable to effectively conduct the beam energy imparted to it then large portion of the current probe remains in the specimen as the electron bean loses all of their initial energy and they remain captured by the specimen [126].
- The charge flows to ground in a conductive specimen but if the ground pathway is broken, conductive specimen quickly accumulates charge and its surface potential rises [126].
- If certain electron holes moves outwards through drift and diffusion along radial direction during transitory charging process [127].

As a result, calculating the crystallite sizes from the Scherrer's equation was considered appropriate for comparative purposes. Irregular clustering of the particles (with large voids between aggregates and mesopores within) was apparent at 600 °C annealed samples (anatase phase). However, for 900 °C annealed samples which consist only of rutile phase, the aggregation completed hence it can be observed that there exist tiny shiny spheroids that are lying on the surface of TiO_2 with clearly defined domain boundaries which grew with an increase in temperature.

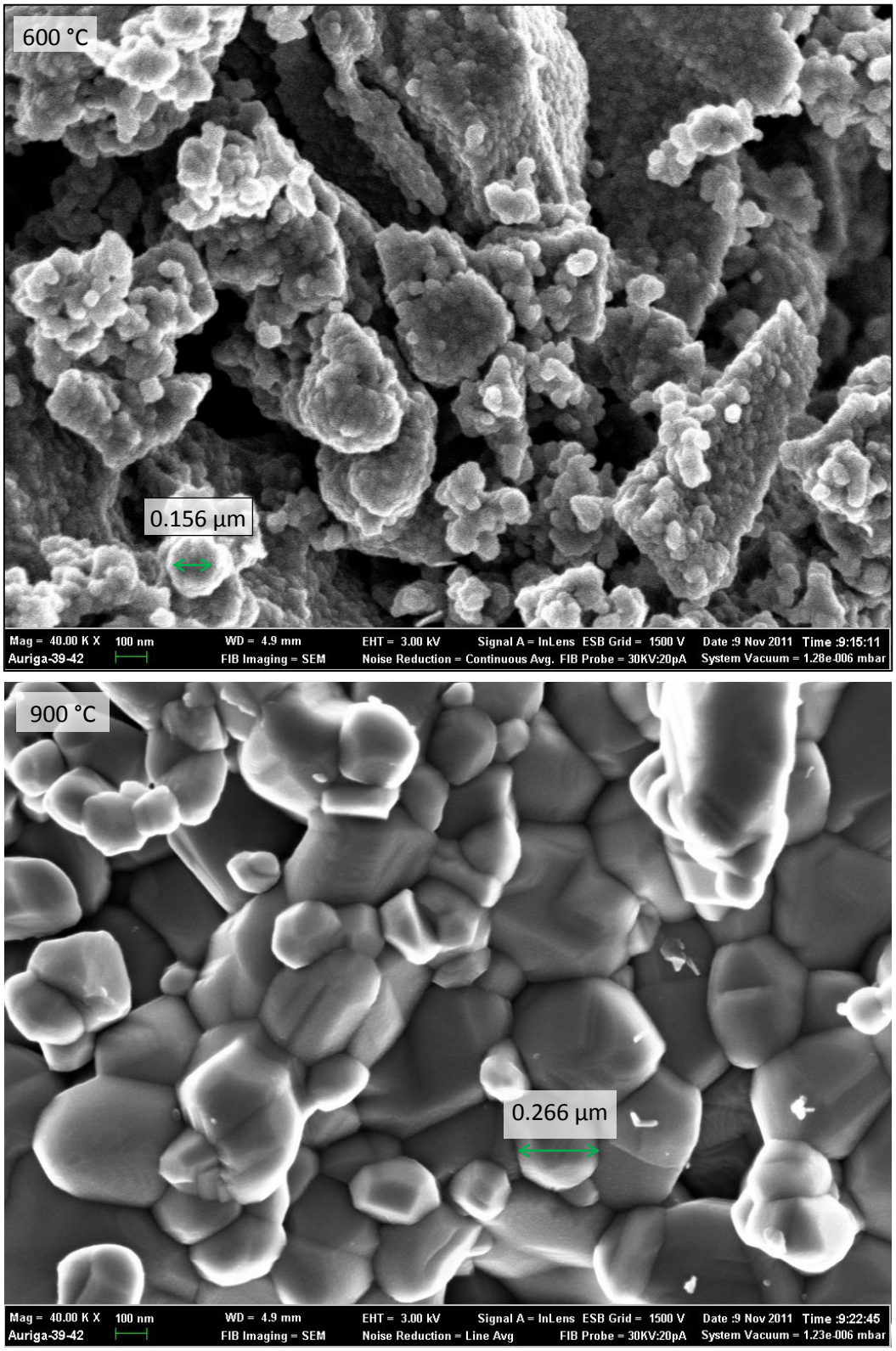

Figure 4.11: SEM images of Au-TiO_2

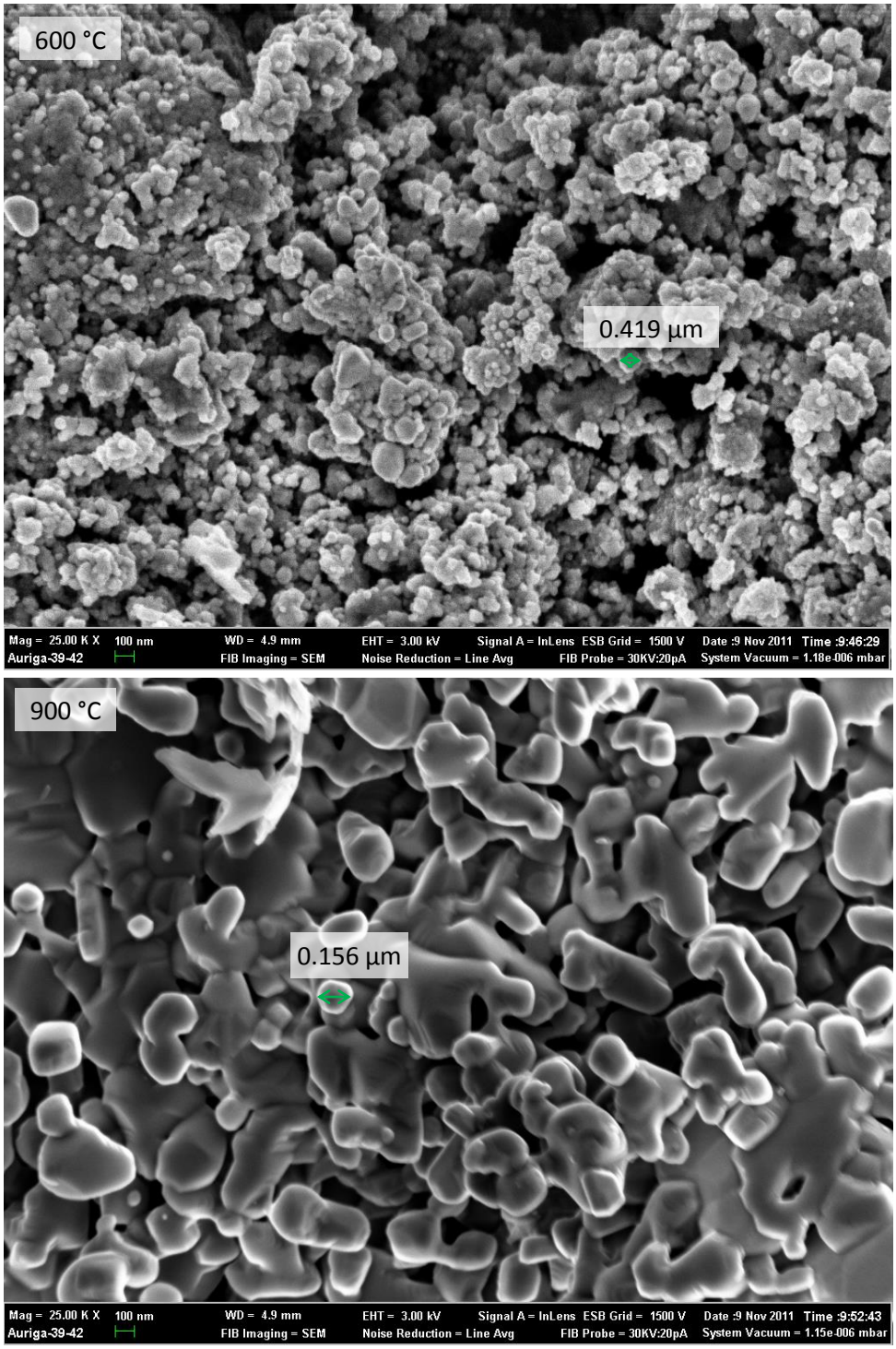

Figure 4.12: SEM images of Au-TiO_2

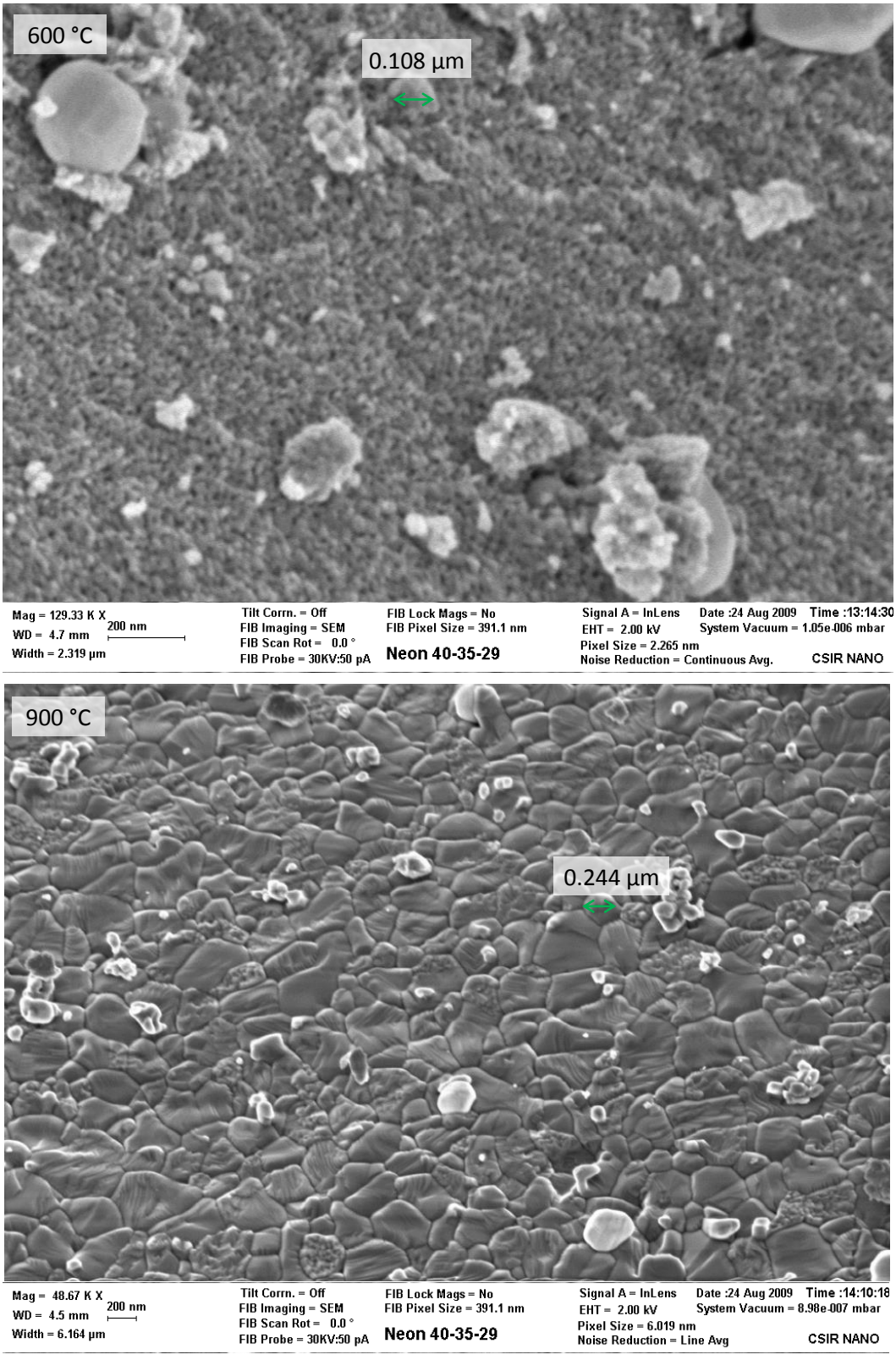

Figure 4.13: SEM images of Au-TiO_2

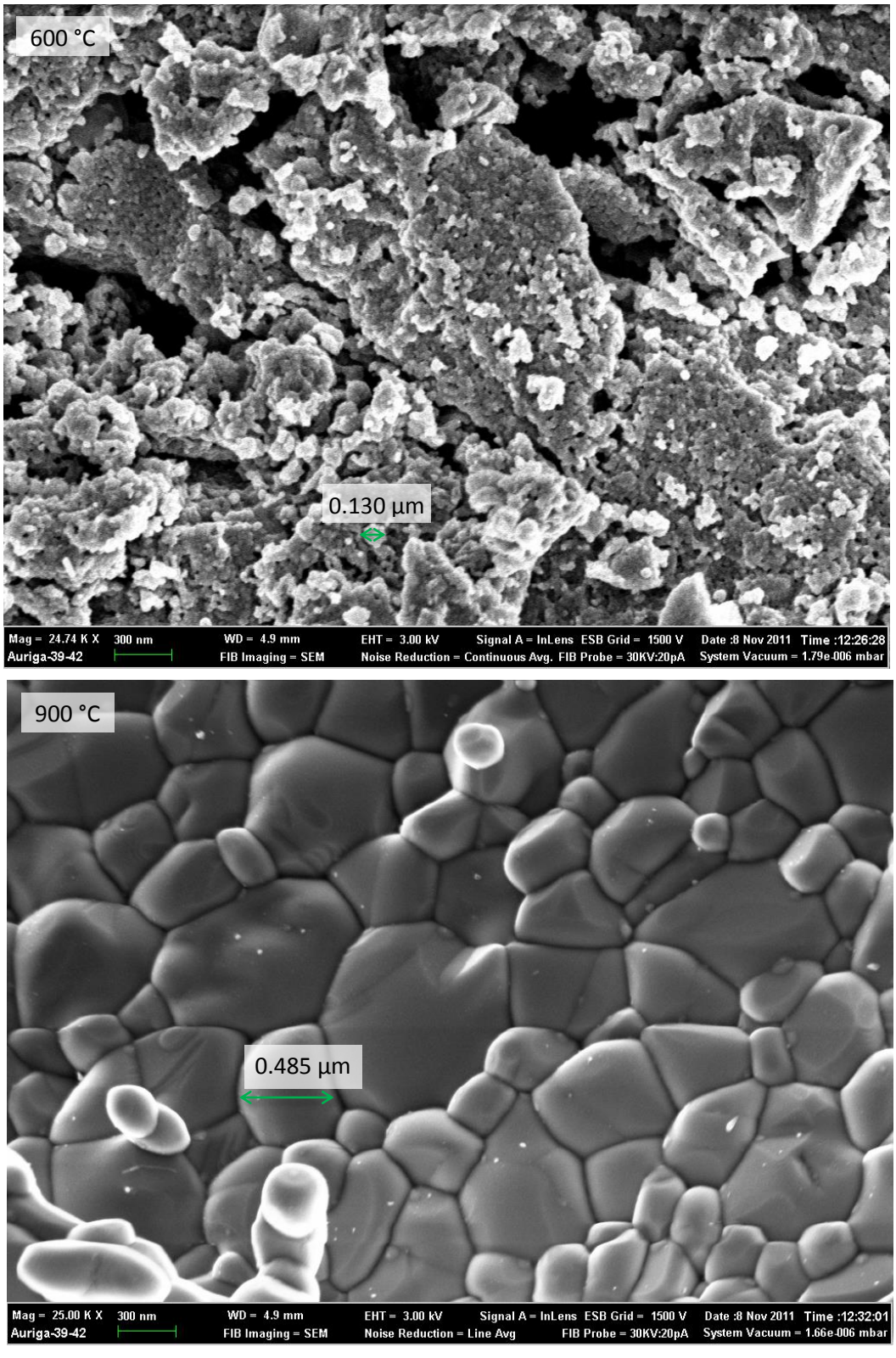

Figure 4.14: SEM images of Au-TiO_2

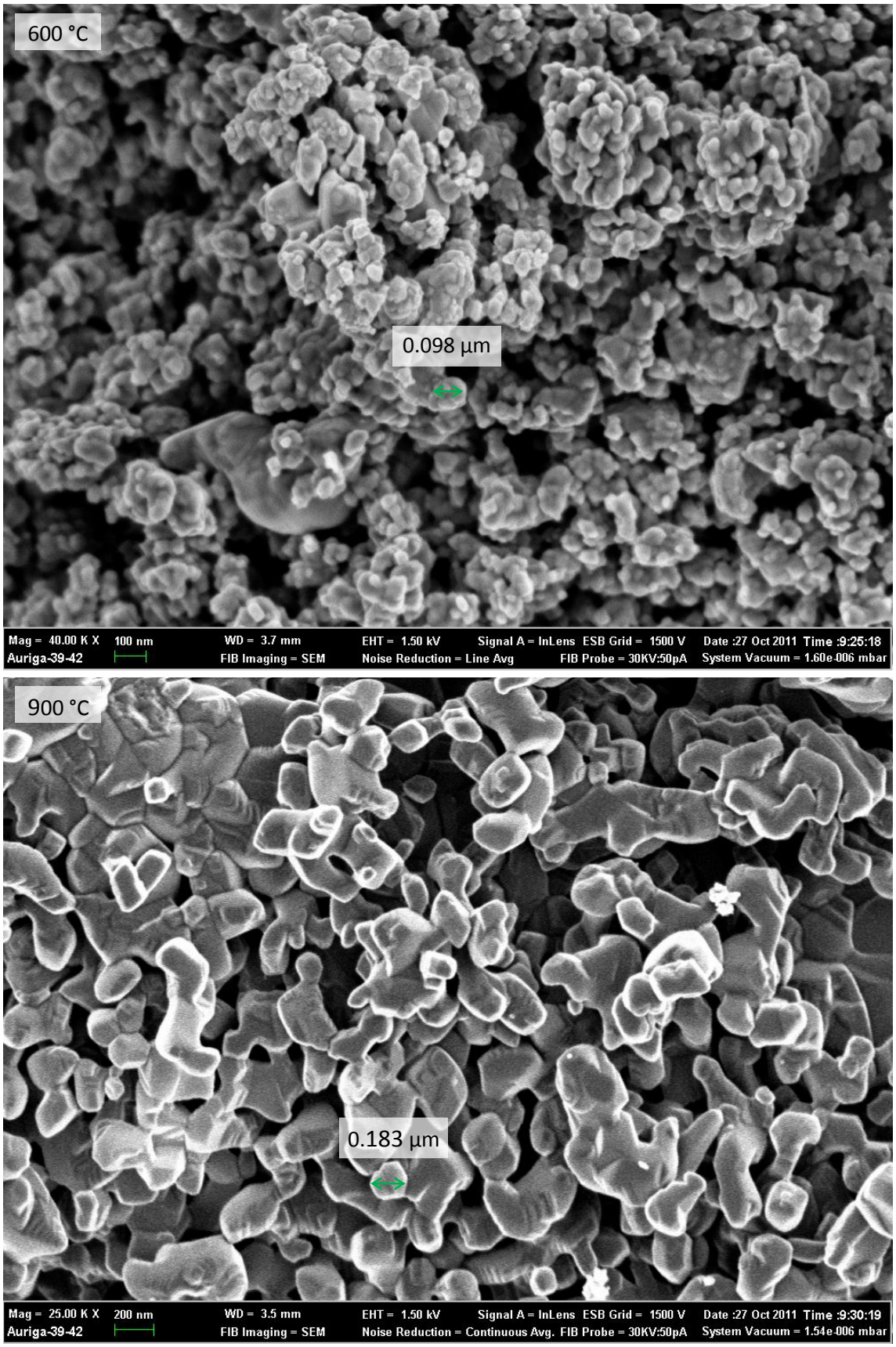

Figure 4.15: SEM images of undoped TiO_2

The estimations of the elemental composition of the various samples was carried out using SEM incorporated EDS and are shown in figure 4.15 (for undoped TiO_2) and 4.16 – 4.19 (for metal loaded samples) at 900 ^{0}C. As can be seen in figures 4.16 - 4.19, the strong Ti and O peaks are observed through all the figures on a predicted 1:2 atomic ratio indicating that TiO_2 is formed [128]. The EDS spectra of metal loaded TiO_2 clearly showed traces of metallic elemental dopants, which indicates that the dopant metals are not integrated in the TiO_2 matrix but are located near the surface regions. The lower intensities of Pd, Ag, Au and Pt signals as compared to those of O and Ti are due to the small amounts of palladium, silver, gold and platinum present in the samples [129]. It can also be observed that there are traces of Cu and Cl peaks attributed to the copper grid and the chlorine ions from the organic compounds used in the preparations. The results agree with the XRD results [129].

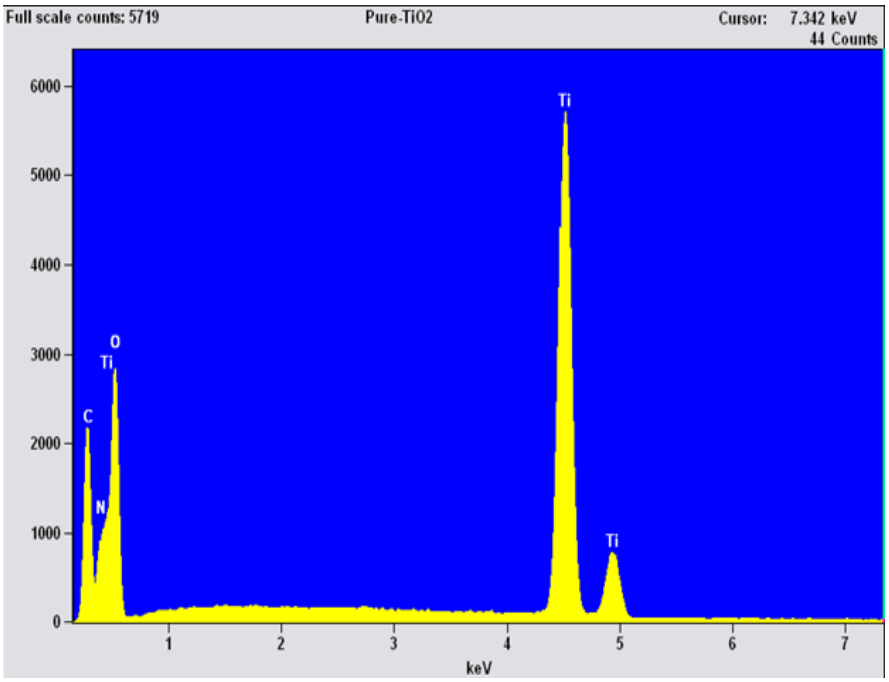

Figure 4.16: EDS spectrum of undoped nanophase TiO_2.

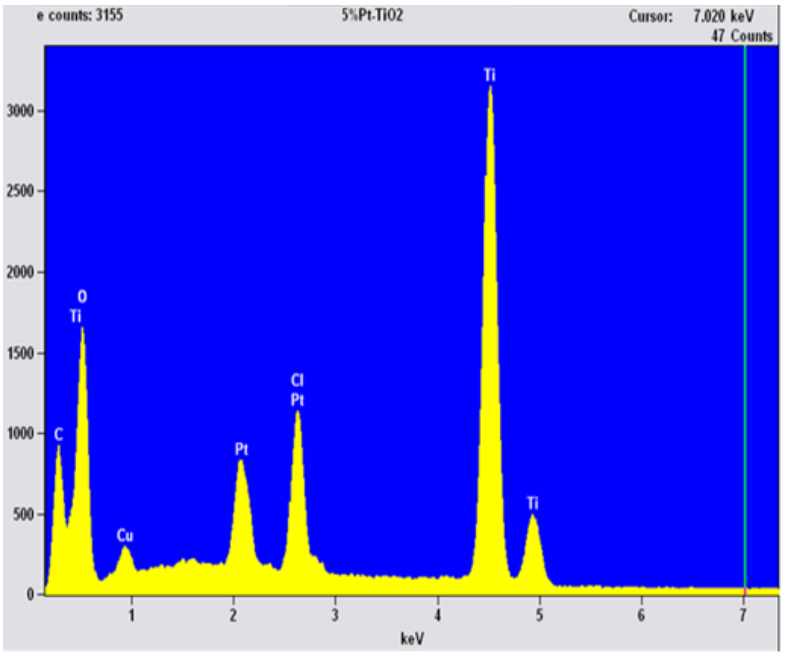

Figure 4.17: EDS spectrum of Pt - TiO_2.

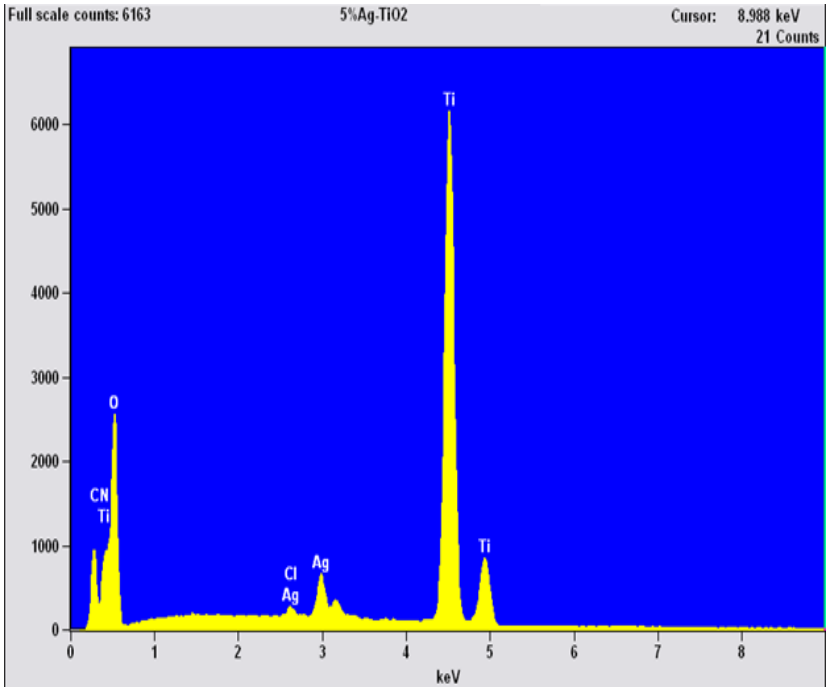

Figure 4.18: EDS spectrum of Ag-TiO_2.

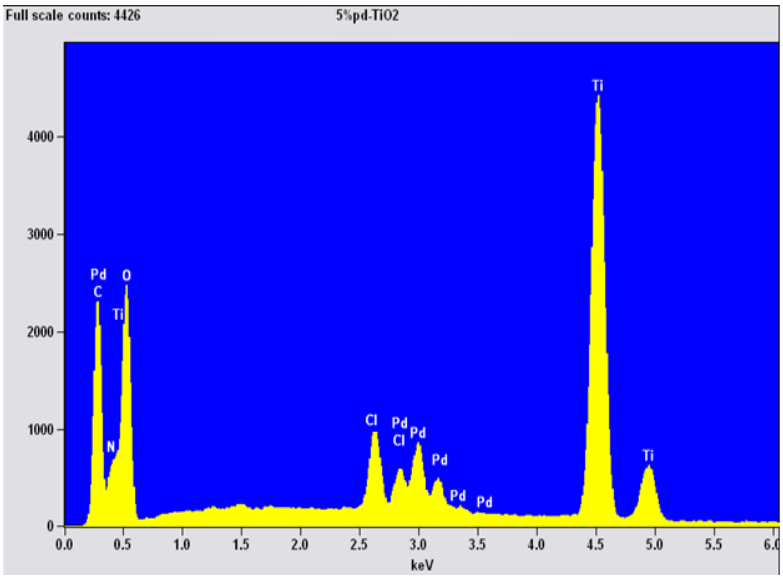

Figure 4.19: EDS spectrum of Pd-TiO_2.

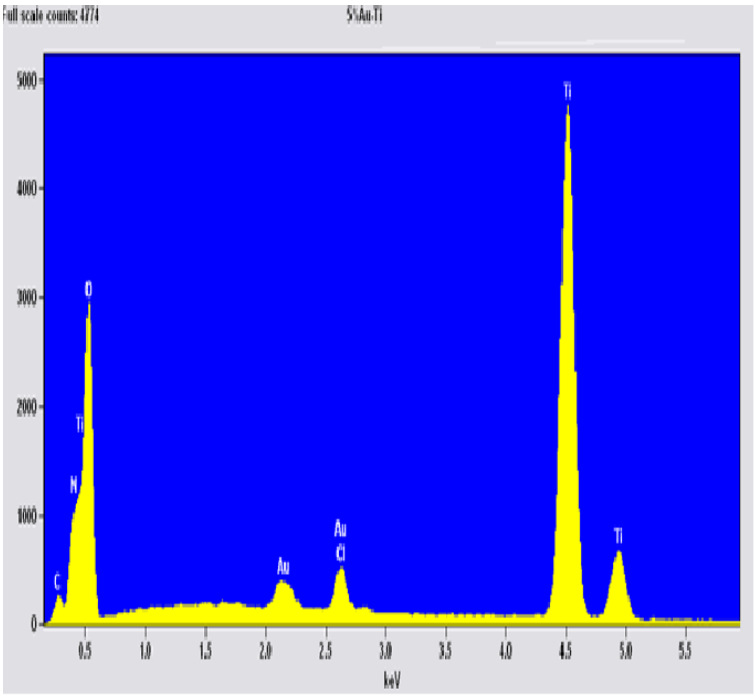

Figure 4.20: EDS spectrum of Au - TiO_2.

4.4 DIFFUSE REFLECTANCE SPECTROSCOPY (DRS) RESULTS

Focus here was on two samples i.e. Au and Pd loaded samples due to erroneous DRS data of Ag and Pt hence they cannot be included in DRS report as time restricts the allowance of another data collection. The UV-VIS DRS spectra of udoped TiO_2 and metal (Au and Pd) loaded TiO_2 are shown in figure 4.20. It is now well established that anatase TiO_2 sample shows intense UV absorption band which is due to the charge-transfer absorption from the oxide anions 2p orbital valence band to the conduction band of 3d orbital of Ti^{4+} cations is below 400 nm which compares well with the findings by Wu *et al*. [130]. As can be seen from the figure, anatase TiO_2 shows almost zero absorption in the visible region.

However, the Pd loaded sample caused a significant increase of the absorption to the visible region because of the surface plasmon absorption of palladium particles [131, 132] . A broad absorption peak between 450–500 nm is observed on the spectrum of Pd-TiO_2. This peak is assigned to the surface plasmon resonance peak of Pd particles indicating that plasmonic palladium nanocrystallites are formed on the surface of TiO_2. This clearly shows the contribution of metallic Pd nanocrystallites. The results are similar to those obtained by Leong *et al*. [131] on their surface deposited Pd-TiO_2.

The Au-loaded sample also shows a significant increase in absorption in the visible region. The spectrum of Au-loaded TiO_2 shows an absorption peak between 550 and 600 nm typically assigned as the surface plasmon resonance peak of metallic Au particles and this indicates the formation of plasmonic gold nanocrystallites onto TiO_2 surface. The finding agrees very well with the work by Rayalua *et al*. [133] , who found similar results on their surface doped (deposited) Au-TiO_2. This further confirms that gold metals prefer surface regions which is consistent with what was found in the XRD and SEM/EDX studies.

At low wavelength below roughly 350 nm it can be observed that there is a similarity in the decline of the three spectrum and absorbance above 400nm to

the entire visible region display that spectra of Au- and Pd-loaded TiO_2 have an effect on absorbance of TiO_2 that can be observed and the results show a red shifted in the absorption edge agreeing well with the report by Lee et al. in (2012) [134]. For the metal loaded samples the considerably large absorption tail in the visible region could be due to oxygen vacancies indicates that various platinum group metals affect the optical properties of light absorption of TiO_2 significantly and agreeing well with observations by Pan and Xu reported in (2013) [135]. This could be due to metals giving rise to localised energy levels in the band gap of TiO_2 into which valence band electrons are excited at wavelengths longer than 400 nm.

The major role of doped metals on TiO_2 is to accelerate the formation of superoxide radical anion O_2 and also to decrease the recombination of electron and hole by scavenging the electrons in the conduction band [6]. Li and Li in (2002) [67] suggested that visible light photosensitivity is due to absorption of light by loaded metals.

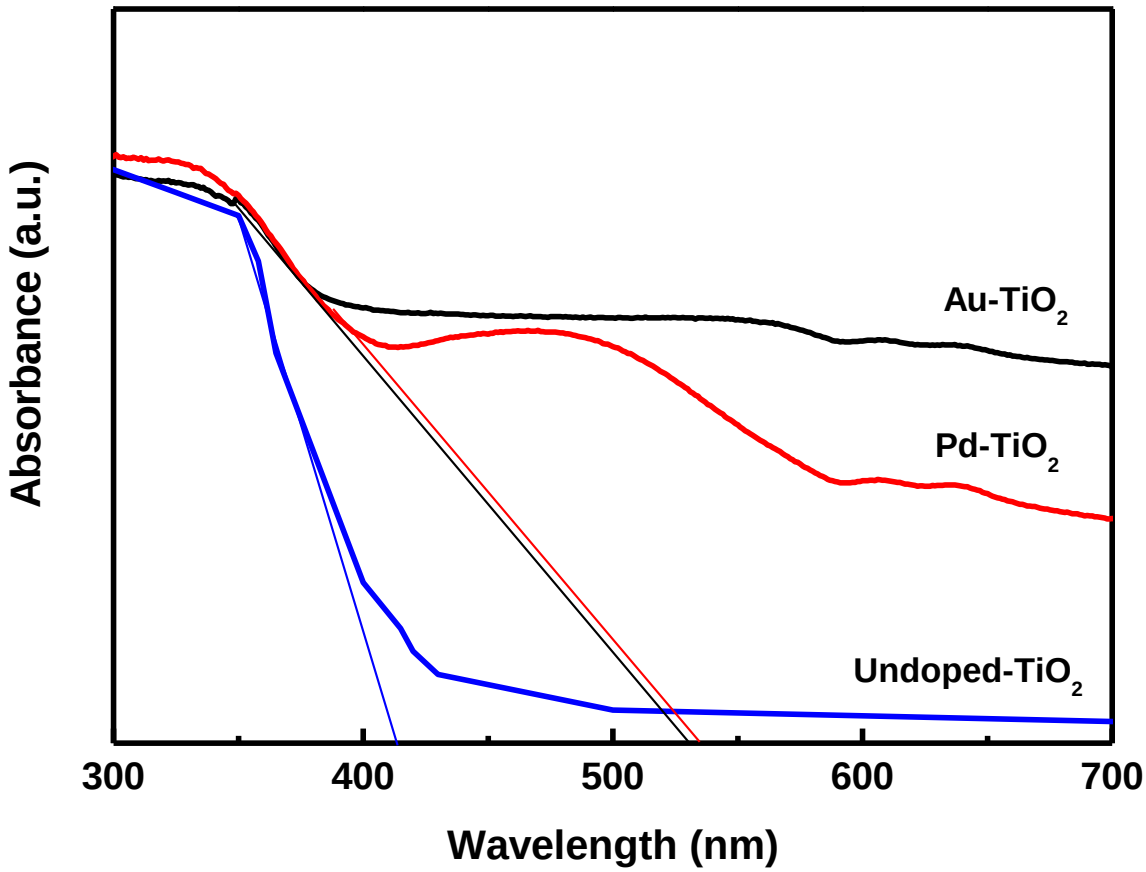

Figure 4.21: UV-VIS DRS spectra of undoped, Au and Pd doped TiO_2 heated at 300 °C.

The optical bandgap (E_g) of the samples was calculated using the Tauc equation [136]

$$E_g = h*c/\lambda = 1239.8/\lambda,$$

where E_g is the bandgap energy (eV), h is the Planck constant, c is a speed of light and $\lambda(nm)$ = cut off wavelength. The cut off wavelength is determined by extrapolating the straight line portion of the UV-VIS plot to intercept the wavelength axes as shown in figure 4.20. These cut-off wavelengths are associated with the absorption edges. The absorption edges and the associated optical bandgaps are shown in table 4.3

Table 4.3: Calculated energy band gaps of pure TiO_2 and metal doped TiO_2.

Sample	Wavelength (nm)	Energy band gap (eV) (± 0.03)[d]
Undoped nano TiO_2 [137]	-	(3.2)
Undoped nano TiO_2	411	3.02
Au-doped TiO_2	528	2.30
Pd-doped TiO_2	534	2.22

An alternative method of determining the bandgaps is by using the Kubelka-Munk relation. In this method, the reflectance is converted into the Kubelka-Munk function (equivalent to the absorption coefficient) $F(R)$, using the relation:

$$\alpha = F(R) = \frac{(1-R)^2}{2R}$$

where R is the reflectance of the sample with respect to a reference at each wavelength and the bandgap energies are estimated from the variation of the Kubelka-Munk function with photon energy.

Anand *et al.* [138] 's procedure of calculating the bandgaps was followed and these researchers used the equation $\alpha = A(hv - E_g)^n/hv$, where α is the absorption coefficient, A is a constant hv is the energy of light and n is a constant depending on the nature of the electron transition in their calculations. The band energy can be obtained from the plots of $[F(R_\infty)hv]^n$ vs hv as the intercept at the $[F(R_\infty)hv]^n$ axis, which is the extrapolated linear part of the plots. Figure 4.22 shows how the bandgaps obtained using this procedure were determined.

For the Au doped TiO_2, the bandgap was found to be 2.30 eV whereas for the Pd-doped was 2.22 eV supported Khan *et al*. report of (2007) were the band gaps were estimated to be 2.82 and 2.32 eV by the same procedure of dropping the line from the maximum slop to the x-axis and very well comparable [139] in addition to those obtained using the Tauc approach [136]; suggesting that the direct and not the indirect transition, is decidedly appropriate in anatase TiO_2 nanocrystallites since their calculated band energy should always be very much less than the anatase bandgap energy as reported by Reddy et al. in (2002) [140].

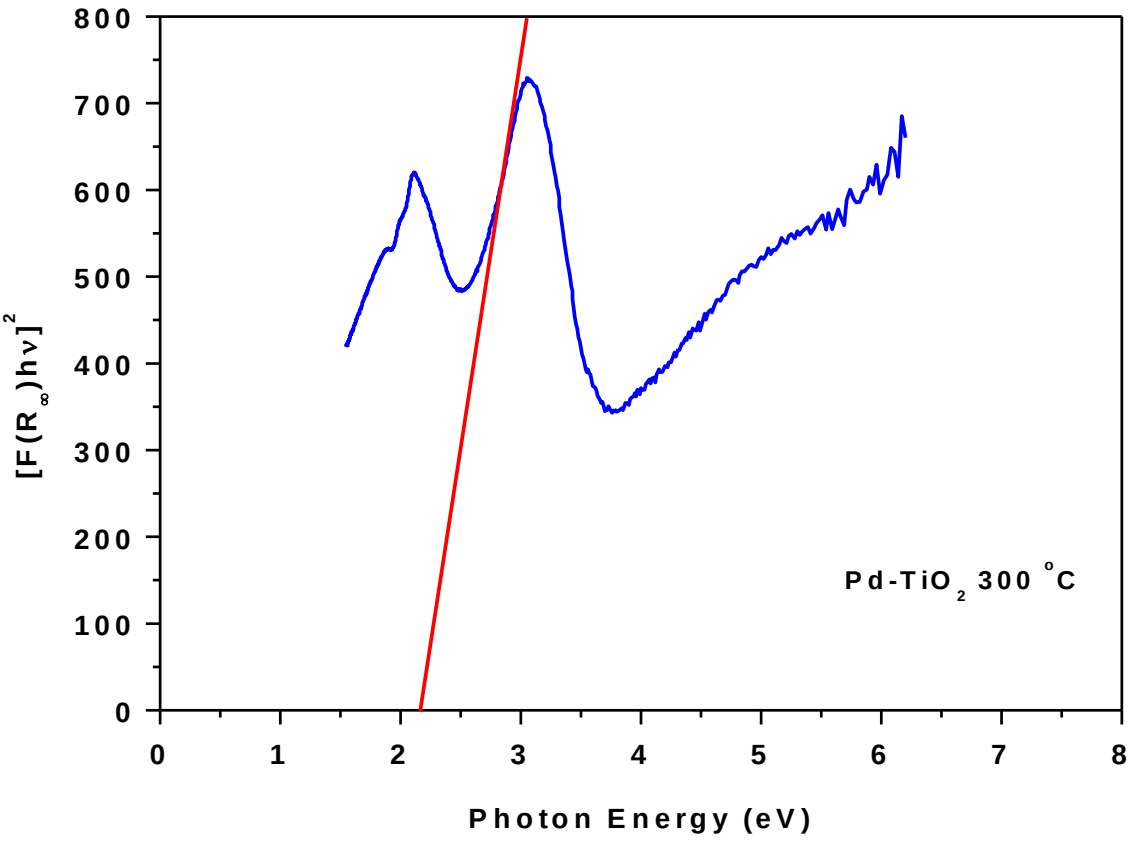

Figure 4.22: The Kubelka-Munk transformed reflectance spectrum of Pd - doped TiO_2 annealed at 300 ^{0}C.

CHAPTER 5

5.1 SUMMARY AND CONCLUSIONS

The metal doped TiO_2 samples were prepared using the standard sol-gel method with TiO_2 and the metal salts being the starting raw materials. The work aimed in investigating structural morphology, location of dopants, optical properties of Au, Pt, Pd, and Ag doped TiO_2. The gelation time was well monitored and dopants concentration was kept constant throughout in all samples with a drying temperature of 100 °C. The reactivity order followed the electronegativity and electron affinity order of the doping metal elements. The characterisation of the prepared catalysts revealed the formation of nano crystallites with controlled sizes. The XRD results indicated that all as-prepared and the 300 °C annealed samples presented an amorphous phase with very weak anatase phase peak.

The effects of dopants on the phase transformation from anatase to rutile were investigated and fully discussed and the study shows that the presence of gold does not affect the anatase to rutile phase transformation temperature, nor does it restrict the grain growth. Silver does restrict the grain growth but does not affect the phase transformation temperature. Platinum reduces the transformation temperature but does not restrict the grain growth. Palladium reduces the transformation temperature and also restricts the grain growth.

The band gap for the single-phase anatase powders of undoped TiO_2 was found to be 3.02 eV. That of the gold and palladium doped (anatase-only) sample, showed a red-shift towards a lower energy gaps of 2.22 and 2.30 eV, respectively. This shows that dopants improve the photo absorptions of titania.

The locations of metal dopants (i.e. Au, Pt, Ag, and Pd) were also studied. XRD profiles show that gold and platinum are present as metals while silver and palladium are initially present in the form of oxides and after annealing at 900 ^oC convert to metals. The SEM-EDS studies corroborated this by showing that

the metals have not entered into the TiO_2 matrix. DRS studies also showed that in the sol-gel prepared metal loaded samples, metals are on the surface regions.

The major conclusion that can be drawn is that the metals have not entered into the TiO_2 lattice. The atomic radii of these metal ions, in their coordination number 6 (as for Ti^{4+} in TiO_2), are larger than that of Ti^{4+}, which means that substitution of Ti^{4+} ion by these ions or metals is highly unlikely. These dopants are most likely found on the surfaces of TiO_2 as metals. From this work, it is concluded that Au, Ag, Pt and Pd doped nano TiO_2 catalysts could be better dopants amongst others for manipulating TiO_2 properties such as transformation, controlling crystallites sizes, narrowing its bandgap and other TiO_2 research applications.

REFERENCES

[1] M. Lazell and P.O' Brien, “Synthesis of CdS nanocrystals using Cadmium Dichloride and Trioctylphosphine Sulfide,” vol. 9, p. 1381, 1999.

[2] Y. Nakaoka and Y. Nosaka, “Electron Spin Resonance Study of Radicals Produced by Photoirradiation on Quantized and Bulk ZnS particles,” vol. 13, p. 708, 1997.

[3] J. H. Adair, T. Li, T. Kido, K. Havey, J. Moon, J. Mecholsky, A. Morrone, D. R. Talham, M. H. Ludwig and L. Wang, “Recent Development in the Preparation and Properties of Nanometer-size Spherical and Platelet-Shaped Particles and Composite Particles,” vol. 23, p. 139, 1998.

[4] A. Hagfeldt and M. Graetzel, “Light-Induced Redox Reactions in Nanocrystalline Systems,” vol. 95, p. 49, 1995.

[5] M. R. Hoffman, S. T. Martin, W. Choi and D. W. Bahnemann, “Environmental Applications of Semiconductor Photocatalysis,” vol. 95, p. 69, 1995.

[6] A. L. Linsebigler, G. Lu and J. T. Yates, “Photocatalysis on TiO2 Surfaces: Principles, Mechanisms. and Selected Results,” vol. 95, p. 735, 1995.

[7] X. Chen and S. S. Mao, “Titanium Dioxide Nanomaterials: Synthesis, Properties, Modifications, and Applications,” vol. 107, p. 2891, 2007.

[8] E. Matijevic, “Monodispersed Colloids: Art and Sciece,” *Langmuir,* vol. 107, p. 12, 1986.

[9] T. Sugimoto, “A Method in Preparation of Monodisperse Particles,” vol. 12, p. 61, 1996.

[10] V. Taghvaei , A. Habibi-Yangjeh and M. Behboudnia, “Simple and Low Temperature Method for Preparation of Nanocrystalline ZnO in Presence of [EMIM][EtSO4] and Their Photocatalytic Activities,” *Int. J. Nanosci. Nanotechnol.,* vol. Vol. 7, no. No. 2, pp. pp. 94-10, 2011.

[11] K. D. Kim and H. T. Kim, “Synthesis of Titanium Dioxide Nanoparticles using a Continuous Reaction Method,” vol. 207, p. 263, 2002.

[12] T. Sugimoto, “Underlying mechanism in size control of uniform nanoparticles,” vol. 309, p. 106, 2007.

[13] J. Livage, M. Henry and C. Sachez, “Sol-gel Chemistry of transition metal oxides,” vol. 18, p. 259, 1988.

[14] T. Van Gestel, C. Vandecasteele, A. Buekenhoudt, C. Dotremont, J. Luytwn, R. Leysen, B. Van der Bruggen and G. Maesc, “Alumina and titania multilayer membranes for nanofiltration: preparation, cheracterization and chemical stability,” vol. 207, p. 73, 2002.

[15] J. H. Jean and T. A. Ring, “Nucleation and Growth of Monosized TiO2 Powders from Alcohol Solution,” vol. 2, p. 251, 1986.

[16] J-L Look and C. F. Zukoski, “Colloidal Stability and Titania Precipitate Morphology: Influence of ashort-Range Repulsions,” vol. 153, p. 461, 1995.

[17] J-L Look and C. F. Zukoski, “Shear induced aggregation during the precipitation of titanium alkoxides,” p. 461, 1992.

[18] D. Vorkapic and T. Matsoukas, “Reversible Agglomeration: A Kinetic Model for the Peptization of titania Nanocolloids,” vol. 214, p. 283, 1999.

[19] R. L. Penn and J. F. Banfield, “Morphology Development and Crystal Growth in Nanocrystalline Aggregates under Hydrothermal Conditions: Insight from Titania,” vol. 63, p. 1549, 1999.

[20] C. J. Barbe, F. Arendse, P. Comte, F. Lenzmann, V. Shklover and M. Gratzel, “Nanocrstalline Titanium Oxide Electrodes for Photovoltaic Applications,” vol. 80, p. 3157, 1997.

[21] H. Zhang and J. F. Banfield, “Thermodynamics Analysis of Phase Stability of Nanocrystalline Titania,” vol. 8, p. 2073, 1998.

[22] H. Zhang and J. F. Banfield, “Size Dependence of the Kinetic Rate Constant for PhaseTransformation in TiO2 Nanoparticles,” vol. 17, p. 3421, 2005.

[23] A. Navrotsky, “Energetics of Nanoparticle Oxides: Interplay Between Surface Energy and Polymorphism,” vol. 4, p. 34, 2003.

[24] P. K. Naicker, P. T. Cummings, H. Zhang and J. F. Banfield, “Characterization of Titanium Dioxide Nanoparticles using Molecular Dynamics Simmulations,” vol. 109, p. 15243, 2005.

[25] L. Braginsky and V. Shklover, “Light Absorption in TiO2 Nanoparticles,” vol. 9, p. 627, 1999.

[26] H. Sato, K. Ono, T. Sasaki and A. Yamagishi, “First-Principle Study of Two-Dimensional Titanium Dioxides,” vol. 107, p. 9824, 2003.

[27] N. Sakai, Y. Ebina, K. Takada and T. Sasaki, “Electronic Band Structure of Titania Semiconductor Nanosheets Revealed by Electrochemical and Photoelectrochemical Studies,” vol. 126, p. 5851, 2004.

[28] T. Sasaki and M. Watanabe, “Semiconductor Nanosheet Crystallites of Quasi-TiO2 and Their Optical Properties,” vol. 101, p. 10159, 1997.

[29] T. Sasaki, M. Watanabe, H. Hashizume, H. Yamada and H. Nakazawa, “Macromolecule-like Aspects for a Colloidal Suspension of an Exfoliated Titanate. Pairwise Association of Nanosheets and DYnamics Reassembling Process Initiated from It,” vol. 118, p. 8329, 1996.

[30] T. Sasaki, “Molecular nanosheets of quasi-TiO2: preparation and spontaneous reasse,bling,” vol. 5, p. 367, 1998.

[31] C. Milton, B.L. Ingram and L.V. Blade, “Kimzeyite, A Zirconium Garnet F-Ronmi Agnet Cocve, Arkansa,” *Journal of the Mineralogical, Society of America,* vol. 46, p. 533, 1961.

[32] B. O'Regan and M. Graetzel, “A low-cost, high-efficiency solar cell based on dye-sensitized colloidal TiO2 films,” vol. 353, p. 737, 1991.

[33] D. Cathen, D. G. Hodes, M. Graetzel, J. F. Guillemoles and I. Riess, “Nature of Photovoltaic Action in Dye-sensitized Solar Cells,” vol. 104, p. 2053, 2000.

[34] J. C. Yu, J. G. Yu and J. C. Zhao, “Enhanced photocatalytic activity of

mesoporous and ordinary TiO2 thin films by sulfuric acid treatment," vol. 36, p. 31, 2002.

[35] J. N. Hart, D. Menzies, Y. B. Cheng, G. P. Simon and L. Spiccia, "Microwave processing of TiO2 blocking layers for dye-sensitized solar cell," vol. 40, p. 45, 2006.

[36] D. Kim, A. Rothschild, D. J. Yang and H. L. Tuller, "Macroporous TiO2 Thin Film Gas Sensor Obtained Using Colloidal Templates," vol. 130, p. 9, 2008.

[37] J. Lukac, M. Klementova, P. Bezdicka, S. Bakardjieva, J. Subrt, L. Szatmary, Z. Bastl and j. Jirkovsky, "Influence of Zr as TiO2 Doping ion on Photocatalytic Degradation of 4-Chlorophenol," vol. 74, p. 83, 2007.

[38] J. Wang, A. K. Mishra, Q. Zhao and L. Huang, "Size effect on thermal stability of nanocrystalline anatase TiO2," vol. 46, p. 255303, 2013.

[39] R. C Garvle, "Stabilization of the Tetragonal Structure in Zirconia Microcrystal," vol. 82, p. 219, 1978.

[40] K.-N. Kumar, "Growth of Rutile Crystallites during the initial stage of Anatase-To-Rutile Transformation in pure Titania and in Titania-Alumina Nanocomposite," vol. 32, p. 873, 1995.

[41] A. A. Gribb and J. F. Banfield, "Particle size effects on transformation kinetics and phase stability in nanocrystalline TiO2," vol. 82, p. 717, 1997.

[42] R. Srinivasan, L. Rice and B. Davis, "Critical Particle Size and Phase Transformation in Zirconia: Transmission Electron Microscopy and X-Ray Diffraction Studies," vol. 73, p. 3528, 1990.

[43] J.-P. Boilot, J. Biteau, F. Chaput, T. Gacoin, A. Brun, B. Darracq, P. Georges and Y. Levy, "Organic-Inorganic Solids by Sol-Gel Processing: Optical Applications," *Pure and Applied Optics: Journal of the European Optical Society Part A,* vol. 7, p. 169, 1998.

[44] T. Jin, S. Inoue, S. Tsutsumi, K.-I. Machida, G.-Y. Adachi, "Luminescence Properties of Lanthanide Complexes Incorporated into Sol-Gel Derived Inorganic-Organic Composite Materials," *Journal of Non-Crystalline Solids,* vol.

223, p. 123, 1998.

[45] M.C. Carotta, S. Gherardi, C. Malagù, M. Nagliati, B. Vendemiati, G. Martinelli, M. Sacerdoti and I.G. Lesci, “Comparison Between Titania Thick Films Obtained Through Sol–Gel and Hydrothermal Synthetic Processes,” *Thin Solid Films,* vol. 515, p. 8339, 2007.

[46] X. Chen, and S.S. Mao, “Titanium Dioxide Nanomaterials: Synthesis, Properties, Modifications, and Applications,” *Chemical Reviews,* vol. 107, p. 2891, 2007.

[47] M. Brunel 1, F.L Luyer, M. Canva, A. Brun, F. Chaput, L. Malier and J.-P. Boilot, “Reverse-Saturable Absorption in Aluminophthalocyanine-Doped Xerogels,” *Applied Physics B,* vol. 58, p. 443, 1994.

[48] A. Saleh, F.A Rasin and M.A Ameen, “TiO2 Nanoparticles Prepared by Sol-Gel,” *Journal of Materials Science and Engineering,* vol. 3, p. 81, 2009.

[49] H. Nguyen-Ngoc and C. Tran-Minh, “Sol–gel process for vegetal cell encapsulation,” *Materials Science and Engineering C,* vol. 27, p. 607, 2007.

[50] S. Wilska, “An X-ray Diffraction Study to Determine the effect of the Method of Preparation upon the Crystal Structure of TiO2,” vol. 8, p. 1796, 1954.

[51] S.-J. Kim, S.-D. Park and Y.H Jeong, “Homogeneous Precipitation of TiO2 Ultrafine Powders from Aqueous TiOCl2 Solution,” *Journal of the American Ceramic Society,* vol. 82 , p. 927, 1999.

[52] D. Dambournet, I. Belharouak and K. Amine, “Tailored Preparation Methods of TiO2 Anatase, Rutile, Brookite: Mechanism of Formation and Electrochemical Properties,” vol. 22, p. 1173, 2010.

[53] W. Li and T. Zeng, “Preparation of TiO2 Anatase Nanocrystals by TiCl4 Hydrolysis with Additive H2SO4,” vol. 6, p. 21082, 2011.

[54] Y. Bessekhouad, D. Robert and J. V. Weber, “Preparation of TiO2 nanoparticles by Sol-Gel route,” vol. 5, p. 153, 2003.

[55] C. Lao, Y. Chuai, L. Su, X. Liu, H. Cheng and D. Zou, “Mix-solventthermal Method for the Synthesis of Anatase Nanocrystalline Titanium dioxide used in

Dye-sensitized solar cell," vol. 85, p. 457, 2005.

[56] R. D. Shannon and J. A. Pask, "Kinetics of the Anatase-Rutile Transformation," vol. 48, 1965.

[57] D. P. Macwan, P. N. Dave and S. Chaturvedi, "A review on nano-TiO2 sol-gel type syntheses and its applications," vol. 46, p. 3669, 2011.

[58] M. S. Nahar, J. Zhang, K. Hasegawa, S. Kagaya and S. Kuroda, "Phase transformation of anatase-rutile crystals in doped and undoped TiO2 particles obtained by the oxidations of polycrystalline sulfide," vol. 12, p. 168, 2009.

[59] G. Q. Li, C. Y. Liu and Y. Liu, "Different effects of cerium ions doping on properties of anatase and rutile TiO2," vol. 253, p. 2481, 2006.

[60] C. G. Wu, C. C. Chao and F. T. Kuo, "Enhancement of the photo catalytic performance of TiO2 catalysts via transition metal modification," vol. 97, p. 103, 2004.

[61] S. Sakthivel, M. V. Shankar, M. Palanichamy, B. Arabindoo, D. W. Bahnemann and V. Murugesan, "Enhancement of photocatalytic activity by metal deposition: characterization and photonic efficiency of Pt,Au and Pd deposited on TiO2 catalyst," vol. 38, p. 3001, 2004.

[62] Y. N. Tan, C. L. Wong and A. R, Mohamed, "An Overview on the Photocatalytic Activity of nano-Doped-TiO2 in the Degradation of Organic Pollutants," p. 18, 2011.

[63] N. Lakshminarasimha, A. D. Bokare and W. Choi, "Effect of Agglomerated State in Mesoporous TiO2 on the Morphology of Photodeposited Pt and Photocatalytic Activity," vol. 116, p. 17531, 2012.

[64] H. Zhang and J. F. Banfield, "Understanding Polymorphic Phase Transformation Behaviour during Growth of Nanocrystalline Aggregates: Insights from TiO2," vol. 104, p. 3481, 2000.

[65] Y. Hu, H-L. Tsai and C-L. Huang, "Effects of Brookite Phase on the Anatase-Rutile Transition in Titania Nanoparticles," vol. 23, p. 619, 2003.

[66] B. Grzmil, M. Glen, B. Kic and K. Lubkowshi, “Study of the anatase to rutile transformation kinetics of the modified TiO2,” vol. 15, p. 73, 2013.

[67] F. B. Li and X. Z. Li, “The Enhancement of Photodegradation Efficiency using Pt-TiO2 Catalyst,” vol. 48, p. 1103, 2002.

[68] B. Cloudhury ans A. Cloudhury, “Local Structure Modification and Phase Transformation of TiO2 Nanoparticles Initiated by Oxygen Defects, Grain size, and Annealing Temperature,” vol. 3, p. 55, 2013.

[69] B. P. Uberuaga and X-M. Bai, “Defects in Rutile and Anatase Polymorphs of TiO2: Kinetics and Thermodynamics near Grain Boundaries,” vol. 23, p. 435004, 2011.

[70] G. Korotcenkov, “The Role of Morphology and Crystallographic Structure of Metal Oxides in Response of Conductometric-type gas Sensors,” vol. 61, p. 1, 2008.

[71] A. Esfandiar, S. Ghasemi, A. Irajizad, O. Akhavan and M. R. Gholami, “The Decoration of TiO2/reduced Graphene Oxide by Pd and Pt Nanoparticles for Hydrogen gas Sensing,” vol. 37, p. 15423, 2012.

[72] A. Hoel, L. F. Reyes, S. Saukko, P. Heszler, V. Lantto and C. G. Granqvist, “Gas Sensing with Films of Nanocrystalline WO3 and Pd made by Advanced Reactive gas Deposition,” vol. 105, p. 283, 2005.

[73] S. K. Hazra and S. Basu, “High Sensintivity and Fast Response Hydrogen Sensors Based on Electrochemically Etched Porous Titania thin Films,” vol. 115, p. 403, 2006.

[74] S. Capone, A. Forleo, L. Francioso, R. Rella, P. Siciliano, J. Spandavecchia, D. S. Presicce and A. M. Taurino, “Solid State gas Sensors: State of the Art and Future Activities,” vol. 5, p. 1335, 2003.

[75] L. M. Gonclaves, V-Z. Bermudes, H. A. Ribeiroa and A. M. Mendes, “Dye-sensitized Solar Cells: A Safe bet for the Future,” vol. 1, p. 655, 2008.

[76] O. O. Kelvine and Ekpunobi, “Fabrication and Characterization of Dye-Sensitized Solar Cells Using Anarcardium Occidentale Sensitizer,” vol. 3, p. 3390, 2012.

[77] S. Y. Huang, G. Schlichtho, A. J. Nozik, M. Graetzel and A. J. Frank, “Charge Recombination in Dye-Sensitized Nanocrystalline TiO2 Solar Cells,” vol. 101, p. 2576, 1997.

[78] R. V. M. Otakwa, J. Simiyu, S. M. Waita and J. M. Mwabora, “Application of Dye Sensitized Solar Cell Technology in the Tropics: Effects of Air Mass on Device Performance,” vol. 2, p. 369, 2012.

[79] G. P. Smestada, S. Spiekermannb, J. Kowalik, C. D. Grantd, A. M. Schwartzbergd, J. Zhangd, L. M. Tolbertc and E. Moons, “A Technique to Compare Polythiophene Solid-State Dye Sentized TiO2 Solar Cells to Liquid Junction Devices,” vol. 76, p. 85, 2003.

[80] R. Daghrir, P. Drogui and D. Robert, “Modified TiO2 for Environmental Photocatalytic Applications: A review,” vol. 52, p. 358, 2013.

[81] M. Ni, M. K. H. Leung and D. Y. C. Sumathy, “A Review and Recent Developments in Photocatalyticwater-splitting using TiO2 for Hydrogen Production,” vol. 11, p. 401, 2007.

[82] A. Zaleska, “Doped-TiO2: Review,” vol. 2, p. 157, 2008.

[83] L. Braginsky and V. Shklover, “Light Absorption at the Interface of Transition-metl Oxide Semiconductor,” vol. 64, p. 15, 2000.

[84] H. Sato, K. Ono, T. Sasaki and A. Yamagishi, “First-Principles Study of Two-Dimensional Titanium Dioxides,” vol. 107, p. 9824, 2003.

[85] K. Ramic, “Physics Department,” 2011.

[86] G. Gouadec and P. Colomban, “Raman Spectroscopy of nanomaterials: How spectra relate to disorder, particle size and mechanical properties,” *Progress in Crystal Growth and Characterization of Materials,* vol. 53, p. 1, 2007 .

[87] E.J. Ayars , C.L. Jahncke, M.A. Paesler and H.D. Hallen , “Fundamental Differences between Micro- and nano-Raman Spectroscopy,” *Jaurnal Microscopy,* vol. 202, p. 142, 2001 .

[88] “http://en.wikipedia.org/wiki/Raman_scattering,” [Online].

[89] D. Shounak, S. Niranjanab, B.S. Satyanarayana and K.M Rao, “Raman Spectroscopy and Conductivity Variation of Nanocluster Carbon thin films grown using a room Temperature based Cathodic arc Process,” *Scientia Iranica,* Vols. Volume 18, Issue 3, June 2011, Pages 797–803, p. P. 797, 2011.

[90] “http://www.solid.ipb.ac.rs/facilities/lab_uraman/index.htm,” [Online].

[91] A. Bogner, P.-H. Jouneau, G. Thollet, D. Basset and C. Gauthier, “A History of Scanning Electron Microscopy Developments: Towards ‘‘wet-STEM’’ imaging,” *Microscopy of Nanostructures,* vol. 38, p. 390, 2007.

[92] J. I. Goldstein and D. B. Williams, “X-ray Microanalysis and Electron Energy Loss Spectrometry in the Analytical Electron Microscope: Review and Future Directions,” *Microbeam Analysis,* vol. 1, p. 29, 1992.

[93] Yu.G. Lavrent’ev, N.S. Karmanov and L.V. Usova, “Electron Probe Microanalysis of Minerals: Microanalyzer or Scanning Electron Microscope?,” *Russian Geology and Geophysics,* vol. 56, p. 1154, 2015.

[94] J. Yang, X.i Li, C. Liu and G. Ma, “Changes of Structure and Eectrical Conductivity of Multi-walled Carbon Nanotubes film Caused by 3 MeV Proton Irradiation,” *Applied Surface Science,* vol. 325, p. 235, 2015.

[95] “http://www.microscopy.ethz.ch/downloads/interactions.pdf,” [Online].

[96] “http://www4.nau.edu/microanalysis/Microprobe-SEM/Instrumentation.html,” [Online].

[97] J.M Parnis and K.B. Oldham∗, “Beyond the Beer–Lambert law: The dependence of absorbance on,” *Journal of Photochemistry and Photobiology A: Chemistry time in photochemistry,* vol. 267, p. 6, 2013.

[98] B.Choudhury, M. Dey and A. Choudhury, “Defect generation, d-d transition, and band gap reduction in Cu-doped TiO2 nanoparticles,” *International Nano Letters,* vol. 3, p. 25, 2013.

[99] V. M. Rammohan, “Modified Beer's Law – Historical Perspectives and Relevance in Near-infrared Monitoring of Optical Properties of Human Tissue,” *International Journal of Industrial Ergonomics ,* vol. 40, p. 125, 2010.

[100] “http://mmrc.caltech.edu/5eadcedd-6a0c-48be-9de7-ab859464f584,” [Online].

[101] “http://mmrc.caltech.edu/5eadcedd-6a0c-48be-9de7-ab859464f584,” [Online].

[102] A. Di Paola, G. Cufalo, M. Addamo, M. Bellardita, R. Campostrini, M. Ischia, R. Ceccato and L. Palmisano, “Photocatalytic Activity of Nanocrystalline TiO2 (Brookite, Butile and Brookite-based) Powders Prepared by Thermohydrolysis of TiCl4 in Aqueous Chloride Solutions,” vol. 317, p. 366, 2008.

[103] J. Yu, H. Yu, B. Chenga and C. Trapalis, “Effects of Calcination Temperature on the Microstructures and Photocatalytic Activity of Titanate Nanotubes,” *Journal of Molecular Catalysis A: Chemical ,* vol. 249, p. 135, 2006.

[104] M. P . Moret, R. Zallen, D. P. Vijay and S. B. Desu, “Brookite-rich Titania Films Made by Pulsed Laser Deposition,” *Thin Solid Films,* vol. 366, p. 8, 2000.

[105] M. S. P. Francisco and V. R. Mastelaro, “Inhibition of the Anatase-Rutile Phase Transformation with Addition of CeO2 to CuO-TiO2 System: Raman Spectroscopy, X-ray Defraction, and Textural Studies,” vol. 14, p. 2514, 2002.

[106] Y Chen, B Zhu, M Yao, S Wang and S Zhang, “The preparation and characterization of Au@TiO2 nanoparticles and their catalytic activity for CO oxidation,” *Catalysis Communications,* vol. 11, pp. 1003-1007, 2010.

[107] M. A. Debeila, M. C. Raphulu, E. Mokoena, M. Avalos, V. Petranovskii, N. J. Coville and M. S. Scurell, “The Effect of Gold on the Phase Transitions of Titania,” vol. 396, p. 61, 2005.

[108] M.J. Uddin, F. Cesano, D. Scarano, F. Bonino, G. Agostini, G. Spoto, S. Bordiga and A. Zecchina, “Cotton textile fibres coated by Au/TiO2 films: Synthesis, characterization and self cleaning properties,” *Journal of Photochemistry and Photobiology A: Chemistry,* vol. 199, p. 64, 2008.

[109] A. K. Datye, J. Bravao, T. R. Nelson, P. Atanasova, M. Lyubovsky and L. Pfefferle, “Catalyst Microstructure and Methane Oxidation Reactivity During the Pd-PdO Transformation on Alumina Supports,” vol. 198, p. 179, 2000.

[110] J. Chen, B. Wiley, J. McLellan, Y. Xiong, Z. Li and Y. Xia, “Optical Properties of Pd-Ag Nanoboxes Synthesized via Galvanic Replacement Reactions,” vol. 5, p.

2058, 2005.

[111] S. Suhonen, M. Valden, M. Pessa, A. Savimaki, M. Harkonen, M. Hietikko, J. Pursiainen and R. Laitinen, “Characterization of Alumina Supported Pd Catalysts Modified by rare Earth Oxides using X-ray Photoelectron Spectroscopy and X-ray Diffraction: Enhanced Thermal Stability of PdO in Nd/Pd Catalysts,” vol. 207, p. 113, 2001.

[112] W. Hung, Y. Chen, H. Chu and T. Tseng, “Synthesis and Characterization of TiO2 and Fe/TiO2 Nanoparticles and their Performance for Photocatalytic Degradation of 1,2-dichloroethane,” vol. 255, p. 2205, 2008.

[113] N. R. C. Raju, K. J. Kumar and A. Subrahmanyam, “Physical Properties of Silver Oxide Thin Film by Pulsed Laser Deposition: Effect of Oxygen Pressure during Growth,” vol. 42, p. 135411, 2009.

[114] S. Sen, S. Mahanty, S. Roy, O. Heintz, S. Bourgenois and D. Chaumont, “Investigation on Sol-Gel Synthesized Ag-doped TiO2 Cermet Thin Films,” vol. 474, pp. 245-249, 2005.

[115] C. Feng, J. Zhang, R. Lang, Z. Jin, Z. Wu and Z. Zhang, “Unusual Photoinduced Adsorption-Desorption Behaviour of Propylene on Ag/TiO2 Nanotube Under Vissible Light Irradiation,” vol. 257, p. 1864, 2011.

[116] M. M. Mohamed and M. S. Al-Sharif, “One Pot Synthesis of Silver Nanoparticles Supported on TiO2 using Hybrid Polymers as Template and its Efficient Catalysis for the Reduction of 4-nitrophenol,” vol. 136, p. 528, 2012.

[117] D.-J. Guo and H.-L. Li, “Electrocatalytic Oxidation of Methanol on Pt Modified Single-walled Carbon Nanotubes,” vol. 160, p. 44, 2006.

[118] A. V. Rosario, E. C. Pereira, “the Role of Pt Addition on the Photocatalytic Activity of TiO2 Nanoparticles: the Limit Between Doping and Metallization,” *Applied Catalysis B: Evironmental ,* vol. 144, p. 840, 2014.

[119] J. Choi, H. Park and M. R. Hoffmann, “Effects of Single Metal-Ion Doping on the Vissible-Light Photo-reactivity of TiO2,” 2009.

[120] B. Donga, B-l. Heb, Y-m. Chaia and C-g. Liu, “Novel Pt nanoclusters/titanium

dioxide nanotubes composites for hydrazine oxidation," *Materials Chemistry and Physics,* vol. 120, p. 404, 2010.

[121] S. Andersson, B. Collen, U. Kuylenstierna and A. Magneli , "phase Analysis Studies on the Titanium-Oxygen system," *Acta Chemica Scandinavica,* vol. 11, p. 1641, 1957.

[122] T. Ohsaka, "Temperature Dependence of the Raman Spectrum in Anatase TiO2," *Journal of the Physical Society of Japan ,* vol. 48, p. 1661, 1980.

[123] H. C. Choi, Y. M. Jung and S. B. Kim, "Size effects in the Raman Spectra of TiO2 Nanoparticles," vol. 37, p. 33, 2005.

[124] U. Balachandran, N. G. Eror, "Raman spectra of titanium dioxide," *Journal of Solid State Chemistry,* vol. 42, p. 276, 1982.

[125] F. Hardcastle, "Raman Spectroscopy of Titania (TiO2) Nanotubular Water-Splitting Catalysts," *Journal of the Arkansas Academy of Science,* vol. 65, p. 43, 2011.

[126] B. Hafner, "http://www.charfac.umn.edu/171DCDA9-0F52-4FBA-96B3-714C63021431/FinalDownload/DownloadId-0648E0FF817A471FA654DDEED05C7599/171DCDA9-0F52-4FBA-96B3-714C63021431/sem_primer.pdf," Characterization Facility, University of Minnesota—Twin Cities , 16 4 2007. [Online].

[127] J. Liu and H.-B. Zhang, "Analysis of microscopic parameters of surface charging in polymercaused by defocused electron beam irradiation," *Micron,* vol. 67 , p. 74, 2014.

[128] G. Wu, T. Nishikawa, B. Ohtani and A. Chen, "Synthesis and Characterization of Carbon-Doped TiO2 Nanostructures with Enhanced Visible Light Response," *Chemistry of Materials,* vol. 19 , p. 4530, 2007.

[129] N. Zhang, S. Liu, X. Fu, and Y.-J Xu, "Synthesis of M@TiO2 (M = Au, Pd, Pt) Core–Shell Nanocomposites with Tunable Photoreactivity," *The Journal of Physical Chemistry C,* vol. 115, p. 9136, 2011.

[130] Z. Wu, Z. Sheng, Y. Liu, H. Wang, N. Tang and J. Wang, "Characterization and

activity of Pd-modified TiO2 catalysts for photocatalytic oxidation of NO in gas phase," *Journal of Hazardous Materials,* vol. 164, p. 542, 2009.

[131] K. H. Leong, H. Y. Chu, S. Ibrahim and P. Saravanan, "Palladium nanoparticles anchored to anatase TiO2 for enhanced surface plasmon resonance-stimulated, visible-light-driven photocatalytic activity," *Beilstein Journal Nanotechnol,* vol. 6, p. 428, 2015.

[132] A. Murphy, "Band-gap Determination from Diffuse Reflectance Measurements of Semiconductor films, and Application to Photoelectrochemical Water-Splitting," *Solar Energy Materials & Solar Cells,* vol. 91, p. 1326, 2007.

[133] S.S. Rayalua, D. Jose, M.V. Joshi, P.A. Mangrulkar, K. Shrestha and K. Klabunde, *Applied Catalysis B: Environmental,* Vols. 142 - 143, p. 142, 2013.

[134] J.S. Lee, K.H. You and C.B. Park, "Highly Photoactive, Low Bandgap TiO2 Nanoparticles Wrapped by Graphene," *Advanced Material,* vol. 24, p. 1084, 2012.

[135] X. Pan and Y.-J. Xu, "Defect-Mediated Growth of Noble-Metal (Ag, Pt and Pd) Nanoparticles on TiO2 wit Oxygen Vacancies for Photocatalytic Redox Reactions under Visible Light," *Physical Chemistry C,* vol. 117, p. 17996, 2013.

[136] J. Dharma, "http://www.perkinelmer.com/Content/applicationnotes/app_uvvisnirmeasurebandgapenergyvalue.pdf)]," PerkinElmer, Inc.. [Online].

[137] A. V. Vorontsov, A. A. Altynnikov, E. N. Savinov and E. N. Kurkin, "Correlation of TiO2 Photocatalytic activity and Diffuse Reflectance Spectra," vol. 144, p. 193, 2001.

[138] G.T.Anand, L.J. Kennedy, J.J. Vijaya, K. Kaviyarasan and M. Sukumar, "Structural, Optical and Magnetic Characterization of Zn1-xNixAl2O4 (0<x<5) Spinel Nanostructures Synthesized by Microwave Combustion Technique," *Ceramics International,* vol. 41, p. 603, 2015.

[139] A. Murphy, "Band-gap Determination from Diffuse Reflectance Measurements of Semiconductor Films, and Application to Photoelectrochemical Water-Splitting,"

Solar Energy Materials & Solar Cells , vol. 91 , p. 1326, 2007.

[140] K.M. Reddy, S.V. Manorama and A.R. Reddy, “Bandgap Studies on Anatase Titanium Dioxide Nanoparticles,” *Materials Chemistry and Physics* , vol. 78, p. 239, 2002.

[141] G. Wu, T. Nishikawa, B. Ohtani and A. Chen, “Synthesis and Characterazation of Carbon-Doped TiO2 Nanostructures with Enhanced Visible Light Response,” *Chemistry of Materials,* vol. 19, p. 4530, 2007.

Publications and Conference Presentations

Publications

Moloantoa RJ, Rammutla KE**,** Mosuang TE, Erasmus RM and Hillie KT,

"XRD, DRS and SEM studies of the effects of metal dopants (Pt and Au) on the structural and optical properties of TiO_2"

Proceedings of SAIP 2011, the 56th Annual South African Institute of Physics Conference, edited by I Basson and AE Botha (University of South Africa,2011), pp.203-206,ISBN: 978-1-86888-688-3,Available online at http://www.saip.org.za

Presentations:

1. The 55th annual conference of the South African Institute of physics (SAIP), CSIR, Pretoria, (2010).

   Moloantoa RJ, Rammutla KE, Mosuang TE and Hillie KT

   "*Structural studies of metal-doped titania systems using XRD and SEM",*

2. The 56th annual conference of the South African Institute of Physics (UNISA, South Africa, 2011).

   Moloantoa RJ, Rammutla KE, Erasmus RM, Hillie KT and Mosuang TE,

   "XRD, DRS and SEM studies of the effects of metal dopants (Pt and Au) on the structural and optical properties of TiO_2"

3. Moloantoa RJ, Rammutla KE**,** Mosuang TE and Hillie KT,

   "Effects of precious metal dopants on the structural and optical properties of TiO_2"

4th International Conference on Nanotechnology and Nanoscience (NanoAfrica 2014 (NanoAfrica 2012) (University of Free State, Bloemfontein, South Africa, April 2012)